

CHANDRA X-RAY OBSERVATORY AND HUBBLE SPACE TELESCOPE OBSERVATIONS OF THE INTERMEDIATE-AGE CLUSTER GLIMPSE-C01

JEREMY HARE,^{1,2} OLEG KARGALTSEV,^{1,2} BLAGOY RANGELOV¹

¹Department of Physics, The George Washington University, 725 21st St, NW, Washington, DC 20052

²The George Washington Astronomy, Physics, and Statistics Institute of Sciences (APSIS)

ABSTRACT

We report the results of *Hubble Space Telescope* (*HST*) and *Chandra X-ray Observatory* (*CXO*) observations of the GLIMPSE-C01 (hereafter GC01) stellar cluster. Color-magnitude and color-color diagrams constructed from PSF-fitting photometry suggest a cluster age of 1-3 Gyrs (although an older age of ~ 10 Gyr cannot be ruled out for low-metallicity), strongly variable $A_V=14-22$, and a distance of 3.2-3.4 kpc. After performing astrometric corrections, we cross-correlate the *CXO* positions of the 15 brightest X-ray sources with the positions of the NIR and optical sources from the *HST* images. We find that nine of these X-ray sources have at least one NIR counterpart within the *CXO* positional error circles. We then use the multi-wavelength properties to identify the nature of the X-ray sources and find an LMXB candidate (source X2), a CV candidate (source X1), and a sub-subgiant/red straggler candidate (source X9). Source X11 is detected during an X-ray flaring episode with a flare luminosity ($L_X = 2.1 \times 10^{33}$ erg s $^{-1}$) and has a quiescent luminosity $L_X < 8.0 \times 10^{30}$ erg s $^{-1}$, in 0.5–8 keV at the distance of GC01. The only potential NIR counterpart of this source lies in the sub-subgiant/red straggler region of the color-magnitude diagram, suggesting that it is in an intermittently accreting LMXB. We also discuss the limits on an intermediate mass black hole at the center of GC01 and the challenges of X-ray source classification imposed by the limitations of the existing data and instrumentation along with future prospects in the *James Webb Space Telescope* era.

1. INTRODUCTION

Thousands of star clusters exist within the Milky Way Galaxy and galactic halo (Scholz et al. 2015). Typically these clusters are classified either as old globular clusters (GCs), which have high concentrations of stars, or less dense open clusters. Open clusters, typically found in the galactic disk, have masses on the order of $10^3 M_\odot$, and ages ranging between $1 < \text{Myr}$ and 1 Gyr, although several old open clusters have also been discovered (e.g., NGC 6791, NGC 188; Kharchenko et al. 2005). Among these are the Young Massive Clusters (YMCs), which are sometimes considered to be a class on their own, with masses $\gtrsim 10^4 M_\odot$ and ages up to a few hundred Myrs (Portegies Zwart et al. 2010). Low-metallicity GCs are mostly found in the Galactic halo (although higher metallicity GCs also exist in the disk) with masses $\sim 10^4\text{--}10^6 M_\odot$ and ages of 8 – 14 Gyrs (see e.g., Fig 9 in Dotter et al. 2010). The GLIMPSE-C01 cluster (GC01, hereafter), which was discovered with *Spitzer* during the Galactic Legacy Infrared Mid Plane Survey (Kobulnicky

et al. 2005), is interesting because it does not fit well into any of these categories.

GC01 is located at $l = 31.3^\circ$, $b = -0.1^\circ$, and lies within 10 pc of the Galactic mid-plane. GC01 was originally estimated to have a mass of $\sim 10^5 M_\odot$, a half-light radius of 36'', and a distance of 3.1-5.2 kpc (Kobulnicky et al. 2005). This cluster is also highly reddened with $A_V \sim 15 \pm 3$, which likely varies across the cluster (Kobulnicky et al. 2005; Ivanov et al. 2005; Davidge et al. 2016).

Since the discovery of GC01, widely varying distance and age estimates have been reported. Both Ivanov et al. (2005) and Davidge et al. (2016) used red clump stars, observed in slightly different filters, to estimate a distance to GC01 of 3.7 and 5.2 kpc, respectively. Davies et al. (2011) used near infrared spectroscopy of 50 stars in the cluster to calculate their velocities and, by assuming that GC01 is moving with the disk, derive a kinematic distance of 5.0 ± 0.9 kpc. The measured velocity dispersion of the stars suggests a virial mass of $(8 \pm 3) \times 10^4 M_\odot$ (Davies et al. 2011).

Due to its centrally-concentrated appearance in the NIR images, GC01 strongly resembles GCs. Therefore,

it was initially suggested that GC01 is a GC with an age of at least a few Gyr. The diffuse infrared emission coincident with GC01 in both *Spitzer* IRAC and MIPS images was interpreted in support of a GC passing through the Galactic disk and interacting with the gas and dust in the disk (Kobulnicky et al. 2005). The advanced age and classification as a globular cluster would be consistent with the lack of radio emission (typically seen in younger open clusters), its high central stellar density, and the large number of giant branch stars with no luminous supergiants (Kobulnicky et al. 2005). However, Davies et al. (2011) found that GC01 is more compact than typical GCs of a similar mass and that the mass density is more similar to that of YMCs. Using the K-band mass-to-light ratio Davies et al. (2011) infer an age between 0.3 and 2 Gyr. Models of the Red Giant Branch (RGB) tip brightness in the color-magnitude diagram (CMD) for stars in GC01 also suggests an age between 1-2.5 Gyr (Davidge et al. 2016). Therefore, GC01 could be a rare intermediate age massive cluster (Davies et al. 2011).

The origin of massive GCs is a matter of ongoing debate (Renaud et al. 2017). It has been suggested that at least some massive GCs in the disk could be the outcome of YMCs evolution (Portegies Zwart et al. 2010). However, GCs could have also coalesced out of a primordial gas cloud that later collapsed into the Galactic disc (see e.g. Krauss & Chaboyer 2003). Furthermore, recent simulations show that low-metallicity GCs may represent the cores of satellite galaxies that merged with the Milky Way (Renaud et al. 2017). If the age of GC01 is indeed substantially less than the age of the Galaxy, its metallicity is closer to solar (Leaman et al. 2013), and its X-ray binary population is different from those in GCs, it may represent a missing evolutionary link between the YMCs and massive GCs.

Studies of X-ray sources located in open and globular clusters are crucial for understanding the evolution, dynamics, and stellar populations of these objects (van den Berg 2013; Pooley 2010, Heinke 2010). Typically, the X-ray populations of globular and aged open clusters consist of cataclysmic variables (CVs), non-accreting¹ millisecond radio pulsars (MSPs), neutron star (NS) or black hole (BH) low mass X-ray binaries which can be in quiescence (LMXBs or qLMXBs, respectively), and active binaries (ABs, such as RS CVn and W Uma type systems; van den Berg 2013; Pooley 2010, Heinke 2010). In dense GCs the relative numbers of these objects are

expected to be related to the number of dynamical encounters (see Pooley & Hut 2006, Heinke et al. 2006, and references therein). In less-dense clusters the X-ray source population is more likely to be primordial in nature (see e.g., Kong et al. 2006, Lan et al. 2010). As a result, GCs tend to be rich with recycled MSPs, many of which are in binaries (e.g., Bogdanov et al. 2006), while in old (> 7 Gyr) open clusters the observed dominating X-ray source population is ABs (see e.g., Vats & van den Berg 2017). If GC01 is indeed an intermediate age massive cluster, the population of X-ray sources would be essentially unknown. This prompted us to carry out multi-band *Hubble Space Telescope* (HST) observations to look for counterparts of the X-ray sources seen in the archival *Chandra X-ray Observatory* (CXO) image of GC01². Below we report the results of these HST observations together with a re-analysis of the archival CXO data and a discussion of the existing limitations and challenges imposed by the current instrumentation.

We present HST and CXO observations, and the data reduction methods in Section 2. In Section 3 we describe the analysis of the CXO and HST data, including the properties of the X-ray sources, NIR/optical photometry, and the cross-correlation of optical/NIR counterparts with the X-ray source positions. We describe the properties of the cluster in Section 4. The multi-wavelength classification of X-ray sources and the limit on the mass of a possible intermediate mass BH (IMBH) are discussed in Section 5. We discuss the current limitations of this study in Section 6 and summarize the results of our findings in Section 7.

2. OBSERVATIONS AND DATA REDUCTION

2.1. HST WFC3/UVIS and WFC3/IR Data

GC01 was observed by HST during a single-orbit visit on 2015 October 5 (GO 14183; see Table 1 for details). The program consisted of imaging observations with the Wide Field Camera 3 (WFC3), using both the Ultraviolet-Visible (UVIS; $162'' \times 162''$ field of view with a $0''.04$ pixel scale) and the Infrared (IR; $136'' \times 123''$ field of view with a $0''.13$ pixel scale) channels. The UVIS F814W (wide *I*) filter and a set of medium NIR filters (F127M, F139M, and F153M) were used (see Figure 1 for filter throughputs). The WFC3/IR data were taken using the timing sequences and sampling parameters give in Table 1. The data were downloaded from the Mikulski Archive for Space Telescopes (MAST³). The final images are produced by PyRAF's *Multidrizzle* task

¹ These MPSs can be solitary, in wide binaries, or in binaries with a very low mass companion which is ablated by the pulsar's wind (i.e., redbacks or blackwidows; for a recent review see Manchester 2017)

² The initial analysis of the CXO data was reported by Pooley et al. (2007).

³ <http://archive.stsci.edu/>

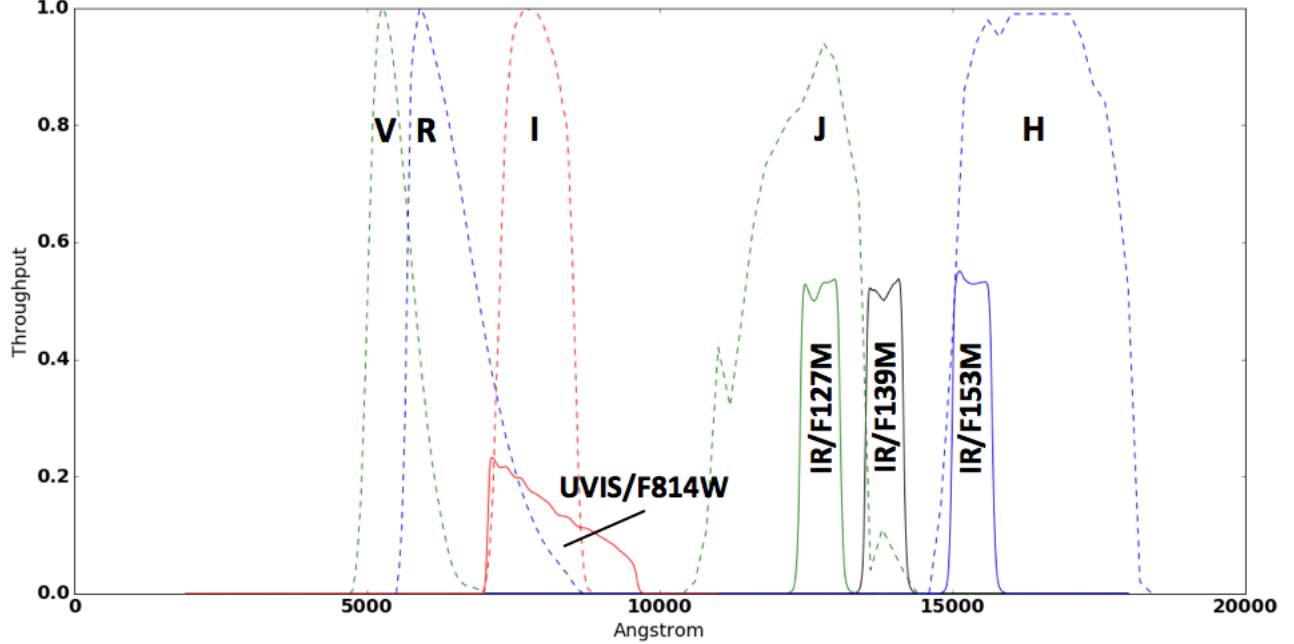


Figure 1. Comparison of the *HST* WFC3 IR and UVIS filters used in this study with Johnson filters.

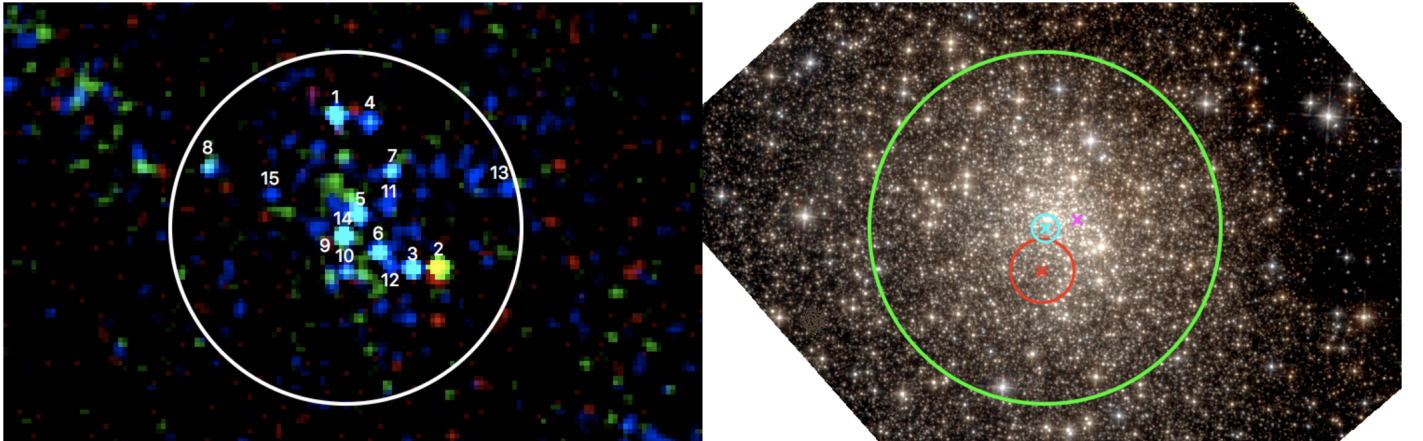


Figure 2. *CXO* and *HST* images of the GC01 field showing the same area on the sky (North is up, East is to the left). The solid white (left) and the green (right) circles represent the 36'' half-light radius reported by Kobulnicky et al. (2005). *Left:* Binned (by a factor of 2) and smoothed (with a Gaussian kernel with a radius of 2''.0) *CXO* false color image (3.0 – 8.0 keV – blue, 1.5 – 3.0 keV – green, and 0.5 – 1.5 keV – red). X-ray sources detected with a significance >6 net counts are numbered in correspondence with Table 2. *Right:* False color *HST* image made from the F127M (blue), F139M (green), and F153M (red) WFC3/IR images. The magenta cross marks the cluster center determined by Kobulnicky et al. (2005). The red cross and circle represent the cluster center and rms error determined using the KDE method, while the cyan cross and circle represent the cluster center and the rms error determined using the isophote fitting method (see Section 4.1).

which aligns images from separate exposures and performs geometric distortion corrections.

The CCDs of the UVIS detector have degraded over time, due to their exposure to high energy particles in low-Earth orbit. This degradation causes streaking (i.e., leakage of the charge from a source pixel into adjacent pixels) in the direction of the readout. The losses in the charge transfer efficiency (CTE) can lead to errors in the photometry and also affects the image qual-

ity. MAST provides UVIS images with the empirically-calculated⁴ CTE corrections applied. We used these CTE-corrected UVIS images for the photometric measurements reported below.

The high density of stars in GC01 makes PSF fitting

⁴ See http://www.stsci.edu/hst/wfc3/ins_performance/CTE/ for more details.

photometry the only robust way to measure the positions and photometric magnitudes of the stars in the cluster. To perform the PSF fitting photometry we used the DOLPHOT⁵ package (Dolphin 2000). DOLPHOT has a number of adjustable parameters, which can influence the photometric measurements. We chose settings similar to those listed in Table 4 of Dalcanton et al. (2012) with the exception of the FitSky parameter value. This parameter fixes how the background is determined for the PSF fit. We adopted FitSky=2 since it is recommended⁶ for crowded fields. We had to apply a number of parameter cuts to the catalog produced by DOLPHOT⁷ to remove the spurious sources and those with inaccurate photometry (e.g., saturated and crowded sources). These cuts were chosen differently for different purposes and the specific choices are described below.

Table 1. *HST* WFC3 exposures

Order	Channel	Filter	Exposure (s)
1		IR F127M	548
2		IR F139M	598
3		IR F153M	598
4	UVIS	F814W	540

NOTE—All exposures were taken within a single *HST* orbit in the order specified in the Table.

2.2. CXO ACIS-S3 Data

We have downloaded and reanalyzed the archival CXO observation of GC01. The data were taken on 15 August 2006 (ObsID 6587) with the Advanced CCD Imaging Spectrometer (ACIS). The exposure time was 45.9 ks and GC01 was imaged on the back-illuminated S3 chip. The detector was operated in full-frame mode, which provides a time resolution of 3.24 s, with the ‘very faint’ telemetry format. We restricted the X-ray data analysis to the standard 0.5–8 keV energy range. To extract the properties of X-ray sources we used the CIAO tools⁸ and the *ACIS Extract*⁹ package (Broos et al. 2010, 2012) for our analysis.

⁵ <http://americano.dolphinsim.com/dolphot/>

⁶ <http://americano.dolphinsim.com/dolphot/dolphot.pdf>

⁷ The electronic version of the catalog is available online.

⁸ Chandra Interactive Analysis Tools (CIAO) version 4.9

⁹ See http://personal.psu.edu/psb6/ACIS/acis_analysis.html for details.

To detect sources in the CXO observation we used *ACIS Extract*, which relies on the Lucy-Richardson image reconstruction algorithm (Lucy 1974) and is optimized for finding faint X-ray sources in crowded fields (Broos et al. 2010). While determining the source position, *ACIS Extract* takes into account the location of the source on the chip and its proximity to other sources. Source positions for uncrowded, on-axis sources (all sources considered below are close to being on-axis) are determined by calculating the centroid of the events. If there are two or more sources near one another, finding the peak in a local maximum-likelihood image reconstruction is the most accurate way to recover the source positions (Broos et al. 2010). This allowed us to accurately recover the positions of sources X9 and X14, which are located only $\sim 0.^{\prime\prime}6$ from each other.

ACIS Extract provides fluxes for all sources, which are calculated by multiplying the median energy of the counts by the number of net counts and dividing by the exposure time and an aperture corrected mean effective area (Broos et al. 2010). For the six sources that have >30 net counts in the 0.5–8.0 keV band, we also extracted the spectra from an $r = 1''$ circular apertures. The spectra were extracted using the CIAO tool `specextract` with an aperture correction applied to the effective area¹⁰. We then fit an absorbed power-law (PL) model to characterize their spectra. No background subtraction was performed because of its negligible contribution (< 10% of the source counts for each of the sources). Due to the small number of counts in all fits, we fixed the hydrogen absorption column to $N_{\text{H}} = 4 \times 10^{22} \text{ cm}^{-2}$, which corresponds to an extinction of $A_V = 18$ (a plausible value for GC01; see Section 4.2) assuming the $N_{\text{H}} - A_V$ relation from Güver & Özel (2009). The X-ray spectra were fit using XSPEC version 12.9.1 (Arnaud 1996).

2.3. Astrometric Corrections

In order to accurately identify the WFC3/IR and UVIS counterparts to the X-ray sources we corrected the absolute astrometry of both the *HST* and CXO images. For the HST images we matched stars from the Two Micron All-Sky Survey catalog (2MASS; Skrutskie et al. 2006; Cutri et al. 2012) to stars in the field of view of the WFC3/IR. We chose 2MASS due to the overlap of the 2MASS and WFC3/IR filters. We then selected 24 stars from the F127M image with bright and unblended 2MASS counterparts. All selected stars are located outside the dense cluster core to avoid source confusion. Prior to the correction, a systematic offset

¹⁰ See <http://cxc.harvard.edu/ciao/threads/pointlike/>

of $0''.37$ ($\Delta\alpha = -0''.37$, $\Delta\delta = 0''.02$) was present between the 2MASS and WFC3/IR stars. We then calculated the astrometric offset between the sources and applied the coordinate transformation to the drizzled images. A subset of 11 of the original 24 WFC3/IR sources, which had unsaturated counterparts in the WFC3/UVIS images, were then used to align the WFC3/UVIS image to the WFC3/IR image.

For *CXO*, we found 10 sources in the 0.5–8 keV band ACIS image with >7 net counts that also had 2MASS counterparts and were located outside of the cluster’s core. We used the CIAO tools `wcs_match` to calculate the astrometric solution and `wcs_update` to apply the coordinate transformation. An offset of $0''.36$ ($\Delta\alpha = -0''.35$, $\Delta\delta = 0''.07$) existed prior to the astrometric correction.

We performed simulations to calculate the statistical uncertainty of the astrometric offsets. We drew source positions from normal distributions with standard deviations equal to the positional uncertainties of the true sources observed by *CXO*, *HST*, and 2MASS. The means of the normal distributions (i.e., representing the source positions at each wavelength) were chosen to be the same between the *CXO* and 2MASS source pairs, as well as the *HST* and 2MASS source pairs. We then introduced a known shift and calculated the offset between the sources 10,000 times. The 1σ uncertainty for the 10 2MASS and *CXO* cross-matched sources is $0''.07$, and the 1σ uncertainty for the 24 2MASS and *HST* cross-matched sources is $0''.02$. Adding these two errors in quadrature gives an astrometric error of $\sim 0''.08$, which we conservatively round up to $0''.1$.

3. DATA ANALYSIS

3.1. X-ray Sources

Source detection was performed using *ACIS Extract* (see Section 2.2), which found 15 X-ray sources with >6 net counts within the cluster half-light radius ($r = 36''$) reported by Kobulnicky et al. (2005). *ACIS Extract* reports the probability (P_B) that counts found within the source aperture come from the background (Broos et al. 2010). Out of 15 X-ray sources numbered in Figure 2 (see left panel), source X8 has the largest $P_B = 7 \times 10^{-5}$. Therefore, all of these sources are confidently detected. The uncertainties of the X-ray source positions are computed from the statistical errors (from centroiding) and systematic errors from the absolute astrometry of *CXO* and *HST* (see Section 2.3) added in quadrature. We consider the 2σ combined statistical and systematic positional uncertainties of the X-ray sources when searching for optical/NIR counterparts. The mean 2σ positional uncertainty is $0''.28$.

For each source, we calculated an unabsorbed X-ray

color defined as $X_{\text{color}} = \log(F_{0.5-2\text{keV}}^{\text{unabs}}/F_{2-6\text{keV}}^{\text{unabs}})$, as well as the unabsorbed X-ray luminosity in the 0.5–8 keV band (see Table 2). The unabsorbed fluxes are calculated using the best-fit photon index (Γ) and the N_{H} adopted above. All fainter sources, that do not pass the number of counts threshold for spectral fitting, have median photon energies > 2.5 keV, suggesting rather hard spectra (see Table 2). Therefore, to calculate the unabsorbed flux and luminosity for these sources we assume $\Gamma = 1.0$, which is the most typical best-fit value obtained for the brighter sources (see Table 2).

Extended emission clearly fills most of the region within the $r = 36''$ half-light radius (see Figure 2). After removing all confidently detected point sources with > 6 net counts, the remaining net count rate within this radius is 0.0125 ± 0.0005 counts s $^{-1}$. However, this emission may not be truly diffuse, but rather composed of faint unresolved point sources. The faintest source in Table 2 has an absorbed limiting flux of 4×10^{-15} erg cm $^{-2}$ s $^{-1}$ in the 0.5–8 keV energy band. This corresponds to an unabsorbed luminosity limit of 8×10^{30} erg s $^{-1}$ at a plausible distance of 3.3 kpc (see Section 4.5), assuming an absorbed power-law model with a photon index $\Gamma = 1$ and hydrogen absorption column $N_{\text{H}} = 4 \times 10^{22}$ cm $^{-2}$. Deeper *CXO* observations with the ACIS-I array (which has significantly lower background compared to ACIS-S3) are needed to probe the fainter end of the X-ray source population in GC01.

3.2. Optical and NIR Photometry with *HST*

To select sources with reliable photometry from the DOLPHOT catalog several quality cuts must be made. The most important quality control parameters for the photometric catalog are the signal-to-noise ratio (SNR), the crowding parameter, the sharpness parameter, and a photometric flag. Only sources with “Photometric Flag” = 0 (i.e., this ensures that sources near the image edge or those with saturated pixels are removed) in each filter were kept for the photometry. The “crowd” parameter shows how much brighter (in magnitude) a star would be if other nearby stars were not fit at the same time, while the “sharp” parameter describes how peaked, compared to the PSF, a source is⁶.

GC01 has both substantial crowding, which affects the photometry, and a large amount of redenning (see Section 4.2). WFC3/UVIS has a higher spatial resolution than WFC3/IR ($0''.04$ versus $0''.13$ pixel scales, respectively), making it better at resolving blended sources. However, UVIS is not able to detect as many sources as WFC3/IR due to the large redenning. For this reason we ran DOLPHOT twice, first using the drizzled F127M image and then using the drizzled F814W image for source detection. Once source detection is complete, DOLPHOT extracts the photometry from the raw

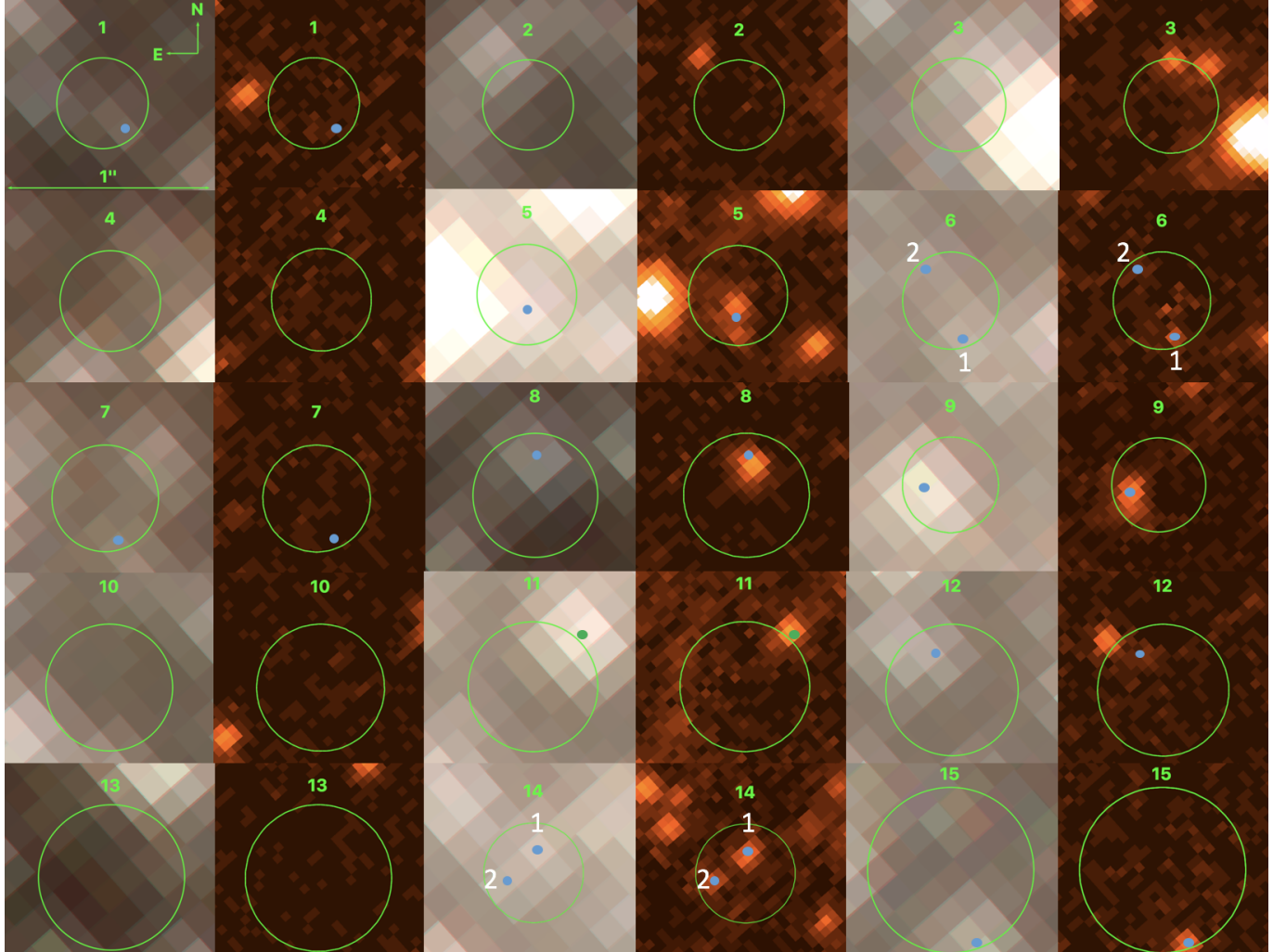


Figure 3. WFC3 NIR and UVIS image cutouts of the vicinity of X-ray sources. North is up and East is to the left. The 2σ X-ray positional error circles are shown in green (see Section 3.1). The NIR images (left columns) are false color (F127M – blue, F139M – green, and F153M – red). The UVIS F814W images (right columns) show the same area of the sky. The blue dots represent the positions of the NIR sources detected in the drizzled WFC3/IR F127M image. In cases with multiple potential NIR counterparts they are numbered (the numbers are used as subscripts to the source names in Table 3). The green dot shows the potential NIR counterpart to the variable source X11, located just outside of the 2σ X-ray position error circle.

frames in each WFC3 filter. Our analysis below focuses primarily on the photometry extracted using the WFC3/IR F127M image for source finding. This is due to the fact that a number of WFC3/IR counterparts to X-ray sources do not have a WFC3/UVIS counterpart. Below, we will explicitly state when the WFC3/UVIS F814W image has been used for source finding.

For the NIR photometry, in addition to requiring “Photometric Flag” = 0, we removed all sources with $\text{SNR} < 4$, $\text{crowd} > 0.2$ and $\text{sharp} > 0.03$ in all WFC3/IR images. We chose all sources within $r = 42''$ of the cluster center (see Section 4.1). The size of the region was chosen to analyze more sources belonging to the cluster, and, at the same time, to avoid the dark patchy areas appearing to the west of the cluster. Below, this region is referred to as the region of interest (ROI). After the cuts to the NIR photometry, 1,964 sources remained within the ROI¹¹.

For the UVIS/NIR photometry using the WFC3/UVIS F814W image for source detection, we used the same ROI and cuts listed above, but also cut all sources with a UVIS SNR < 4 , $\text{crowd} > 0.2$, and $\text{sharp} > 0.1$ leaving 794 UVIS/NIR sources¹¹.

3.3. Optical and NIR Counterparts to X-ray Sources

The confidences of the NIR source detections may be significantly impacted by the unaccounted for systematic uncertainties in the background measurements due to the large amount of crowding in this field. Therefore, to ensure that the NIR counterparts to X-ray sources were confidently detected, we required that they have $\text{SNR} > 30$ in each of the three WFC3/IR filters. Any source meeting the $\text{SNR} > 30$ requirement in all of the F127M, F139M, and F153M images, and located within the 2σ error circle of an X-ray source listed in Table 2 is considered to be a potential counterpart to the corresponding X-ray source (see Figure 3 and Table 3). The only exception is made for source X11, because it is highly variable in X-rays and has a $\text{SNR} > 30$ counterpart just outside of its error circle. Most of the considered X-ray sources are located in the crowded core of GC01, meaning that their NIR counterparts have large crowding values (i.e., > 0.2), with the exceptions of X8, X9, and X11. In Table 3, we only provide F814W photometry for the counterparts of NIR sources detected with $\text{SNR} > 10$ in the F814W image. The lower threshold for the SNR is enabled by the higher resolution of the F814W image.

We find that nine X-ray sources (excluding X11) have at least one NIR counterpart, while three of these X-ray

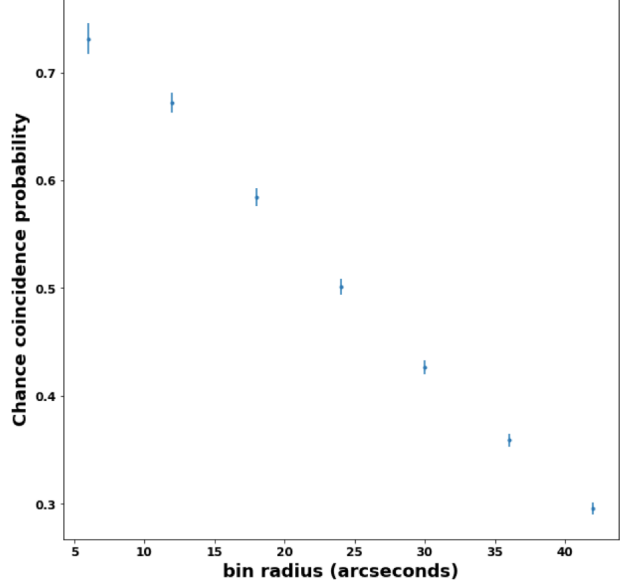


Figure 4. Chance coincidence probability for a NIR source to fall into the mean 2σ X-ray positional error circle ($\delta r = 0''.28$) as a function of distance from the cluster center. The bins span a range between $0'' < r < 42''$ in steps of $6''$.

sources (X5, X6, X14) have two counterpart candidates within their X-ray error circles (see Figure 3). For these three sources, the NIR counterparts are referred to by using a subscript after the X-ray source name (e.g., X6₁, X6₂). Since we used the NIR image as the source detection image, the two NIR sources within the X-ray error circle of source X5 were not resolved and were considered a single NIR source (although they are resolved in the F814W image). In addition, there are also two X-ray sources (X3 and X12) with optical/NIR sources located just outside of the X-ray error circle. These NIR sources are not included in Table 3, but associations with these NIR sources cannot be completely ruled out until more accurate X-ray source positions are obtained in a deeper CXO observation.

The fact that several X-ray sources have two NIR counterparts is not surprising given the high density of NIR sources in the cluster’s core. We estimate the chance coincidence probability of finding a NIR source within the 2σ mean ($\delta r = 0''.28$) positional error circles of the X-ray source as a function of the distance from the cluster center. First, we apply the same cuts to the photometric catalog ($\text{SNR} > 30$ in all WFC3/IR filters) as for the counterpart matching. Second, we divide the $r < 42''$ ROI into seven $6''$ -wide concentric annuli. The density of NIR sources, ρ , within the annuli are computed, giving a range $1.4 < \rho < 5.3$ sources arcsec^{-2} . Next, we calculate the probability of having one or more sources within a randomly placed $0''.28$ radius circle, $P = 1 - \exp(-\rho\pi\delta r^2)$. The chance coinci-

¹¹ The photometry of these sources is provided as an online catalog.

dence probability, ranging from $P = 73\%$ near the cluster core to $P = 30\%$ at the outskirts of the cluster, is shown as a function of distance from the cluster center in Figure 4. Note that most of the X-ray sources fall within the first four annuli (i.e., between $r = 0''$ and $r = 24''$).

Deeper *CXO* observations would allow us to obtain more accurate X-ray source positions and lower the chance coincidence probability. For instance, if the X-ray source positional uncertainties were as low as $\delta r = 0''.1$ the NIR confusion probabilities would drop by a factor of ~ 5 .

Table 2. X-ray sources detected with > 6 net counts in the ACIS-S3 image within the $42''$ ROI.

Source	R.A.	Decl.	δr^a	Net Counts	F_X^b	L_X^c	X_{color}^d	E_{med}^e	Γ^f	C-stat/d.o.f.
X1	282.209462	-1.491307	0.23	61 ± 8	3.6 ± 0.5	9.1	-0.1	4.1	0.9 ± 0.4	67.00/58
X2	282.203688	-1.499904	0.22	52 ± 7	$1.2_{-0.2}^{+0.3}$	340	2.1	1.8	5.6 ± 0.6	24.44/42
X3	282.205215	-1.500029	0.23	39_{-6}^{+7}	2.4 ± 0.4	4.9	-0.3	4.2	0.7 ± 0.4	53.54/39
X4	282.207574	-1.491672	0.25	34 ± 6	2.2 ± 0.4	3.7	-0.8	4.4	-0.2 ± 0.6	34.70/32
X5	282.208201	-1.496848	0.25	31_{-5}^{+6}	2.0 ± 0.4	4.4	-0.3	4.2	1.2 ± 0.5	29.97/28
X6	282.207103	-1.499042	0.24	30_{-5}^{+6}	$1.8_{-0.3}^{+0.4}$	4.5	-0.1	4.0	1.1 ± 0.6	37.07/25
X7	282.206333	-1.494469	0.27	20_{-4}^{+5}	1.3 ± 0.3	2.8	... ^g	4.3	1.0^h	...
X8	282.216777	-1.494315	0.31	14 ± 4	0.6 ± 0.2	1.7	-0.1	3.4	1.0^h	...
X9	282.209069	-1.498165	0.23	10_{-3}^{+4}	0.8 ± 0.3	3.0	0.4	2.6	1.0^h	...
X10	282.208920	-1.500203	0.31	9_{-3}^{+4}	$0.4_{-0.1}^{+0.2}$	0.9	... ^g	3.2	1.0^h	...
X11	282.206564	-1.496531	0.32	9_{-3}^{+4}	$0.5 \pm 0.2(100)^i$	$1.1(210)^i$	-0.3	3.8	1.0^h	...
X12	282.206393	-1.499782	0.32	8 ± 3	$0.4_{-0.1}^{+0.2}$	0.9	... ^g	3.4	1.0^h	...
X13	282.199781	-1.495440	0.36	7 ± 3	$0.4_{-0.1}^{+0.2}$	0.8	... ^g	3.8	1.0^h	...
X14	282.208978	-1.498018	0.24	7 ± 3	$0.8_{-0.3}^{+0.4}$	1.7	... ^g	3.1	1.0^h	...
X15	282.213183	-1.495756	0.40	6_{-2}^{+3}	$0.4_{-0.1}^{+0.2}$	0.8	... ^g	3.8	1.0^h	...

^aX-ray 2σ position error circle radius in arcseconds.

^bObserved 0.5–8 keV flux in units of 10^{-14} erg cm $^{-2}$ s $^{-1}$.

^cUnabsorbed 0.5–8 keV luminosity in units of 10^{31} erg s $^{-1}$ at $d = 3.3$ kpc.

^dX-ray color defined as $X_{\text{color}} = \log(F_{0.5-2\text{keV}}^{\text{unabs}}/F_{2-6\text{keV}}^{\text{unabs}})$.

^eMedian photon energy in the 0.5–8 keV band.

^fBest fit photon index for the absorbed power-law model with abundances from [Anders & Grevesse \(1989\)](#).

^gSources have no counts detected in the soft (0.5–2.0 keV) band.

^hPhoton index set to $\Gamma = 1.0$ for sources with < 30 counts.

ⁱAverage and peak (during the 200 s flare, in brackets) observed flux and unabsorbed luminosity in the 0.5–8 keV band, assuming $d = 3.3$ kpc (see Section 4.5).

4. PROPERTIES OF THE GLIMPSE-C01 CLUSTER

In this section we determine the position of the cluster’s center and then use the photometry to produce the color-color diagram, CMDs, and set constraints on GC01’s distance, age, and extinction. All isochrones are adopted from [Marigo et al. \(2017\)](#) and are re-

calculated for the three *HST* WFC3/IR filters and the WFC3/UVIS filter¹². Finally, we show that the puzzling ‘loopl like structure’ reported by [Kobulnicky et al. \(2005\)](#) is comprised of stars unresolved in shallower survey images.

¹² See <http://stev.oapd.inaf.it/cgi-bin/cmd> for details.

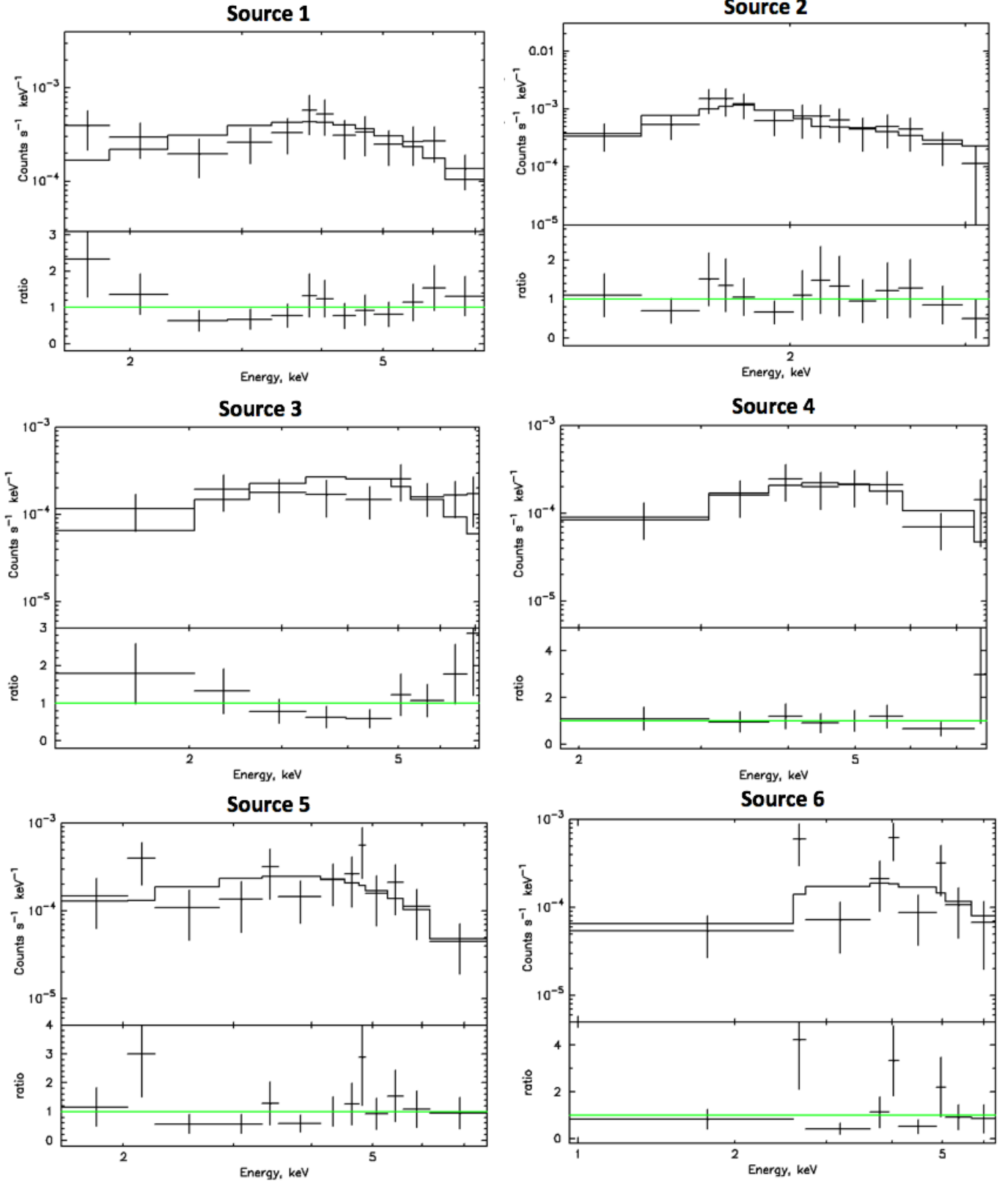


Figure 5. X-ray spectra for six sources detected with > 30 counts. All sources are fit with an absorbed power-law model with fixed $N_{\text{H}} = 4.0 \times 10^{22} \text{ cm}^{-2}$. The fits were performed using Cash statistics (c-stat) using unbinned data (the spectra are binned for visualization purposes only). The best-fit parameters are given in Table 2.

Table 3. Potential NIR counterparts to X-ray sources and their magnitude in the WFC3 IR and UVIS filters (see Section 3.3 for details).

Source	RA	DEC	m_{F814W}^a	Δm_{F814W}^b	m_{F127M}	Δm_{F127M}^b	m_{F139M}	Δm_{F139M}^b	m_{F153M}	Δm_{F153M}^b
X1	282.209434	-1.491339	21.184	0.032	20.383	0.022	19.556	0.016
X5 ^c	282.208204	-1.496877	24.229	0.070	17.228	0.004	16.530	0.003	15.852	0.003
X6 ₁	282.207082	-1.499093	24.598	0.092	18.284	0.006	17.554	0.005	16.826	0.004
X6 ₂	282.207137	-1.498999	19.135	0.010	18.439	0.008	17.764	0.006
X7	282.206317	-1.494525	20.597	0.024	19.587	0.015	18.699	0.011
X8	282.216775	-1.494257	23.998	0.059	19.242	0.010	18.649	0.008	18.035	0.006
X9 ^d	282.209104	-1.498178	23.435	0.041	16.478	0.002	15.652	0.002	14.848	0.001
X11 ^{d,†}	282.206500	-1.496457	23.314	0.039	16.486	0.002	15.646	0.002	14.832	0.001
X12	282.206414	-1.499733	19.477	0.013	18.792	0.011	18.141	0.009
X14 ₁	282.208970	-1.497989	24.099	0.063	18.102	0.006	17.419	0.005	16.800	0.004
X14 ₂	282.209016	-1.498029	24.527	0.085	18.909	0.009	18.272	0.008	17.676	0.007
X15	282.213147	-1.495857	23.809	0.052	18.078	0.005	17.387	0.004	16.687	0.003

^aUVIS magnitude for sources detected with $\text{SNR} > 10$.

^bThe magnitude uncertainties are statistical only and do not include systematic errors due to crowding.

^cThe source is resolved into two individual sources in the higher resolution UVIS image.

^dThis NIR/optical source lies just outside of the X-ray positional error circle. However, due to the highly variable nature of this X-ray source we consider it as a potential NIR/Optical counterpart.

[†]Unlike other sources, this source meets the criteria to be included in the photometric catalog (i.e., $\text{SNR} > 4$, $\text{crowd} < 0.2$, and $\text{sharp} < 0.03$).

NOTE—All magnitude are in the VEGAMAG system.

4.1. Cluster Center and Size

We determined the cluster’s center using two different methods. The first method calculates the peak of the stellar density distribution in the WFC3/IR F127M image using a gaussian kernel density estimator (KDE). Before applying this method we removed all NIR sources with $\text{SNR} < 4$, and did not make a cut on the `crowd` parameter because we only needed confidently detected sources and not their precise photometry. The bandwidth parameter, which controls the variance of the gaussian kernel being used, was the primary source of uncertainty for this method. We tried a number of different¹³ values between 0.1 and 1.0 and found the mean cluster center to be at $\alpha = 282.2091^\circ$ and $\delta = -1.5001^\circ$ with an rms error of $6.5''$.

We also used an alternative method to calculate the cluster center where we fit ellipses to the isophotal contours (isophotes) of the cluster and found their centers. To calculate the isophotes we used the drizzled

WRC3/IR F127M filter image, because it is less affected by reddening than the UVIS image. We then fit 16 ellipses with semi-major axes ranging between $a = 10''$ and $40''$. For $a < 10''$ the isophotal shapes are too amorphous to accurately find the center by fitting an ellipse, while for $a > 40''$ the dust lanes to the west of the cluster begin to affect the isophotes and cause a systematic shift in the centers of the ellipses. The mean position of these ellipses were found to be $\alpha = 282.2089^\circ$ and $\delta = -1.4977^\circ$ with an rms error of $2.8''$. This position differs from the one determined with the first method by $9''$ and by $3''$ from the position reported by Kobulnicky et al. (2005) (see Figure 2).

We did not attempt to calculate the half-light radius of GC01 because the relatively small field of view of the WFC3 detectors prevents an accurate estimation of the background light. The background measurements can have a large impact on the half-light radius estimate. For instance, Kobulnicky et al. (2005) reported a half-light radius of $36''$, while Davies et al. (2011) found a half-light radius of $14''$ and suggested that this difference could come from the estimate of the large amount of background light. In this paper we adopt the half-light radius value of $36''$ reported by Kobulnicky et al. (2005).

¹³ We found that values below 0.1 under-smoothed the data leading to many peaks, while values greater than 1.0 gave consistent results regardless of kernel size, suggesting that the data had been over-smoothed.

4.2. A_V from Color-Color Diagram

In order to determine the extinction¹⁴ in the direction of GC01 we have plotted the F127M–F153M vs. F139M–F153M color-color diagram (see Figure 6). The red star and the error bar represent the mean and standard deviation of the color-color distribution. The 1σ standard deviations are 0.30 for the F127M–F153M and 0.15 for the F139M–F153M colors. To estimate the extinction, we used 500 Myr, 1, 2, and 3 Gyr solar metallicity isochrones, as well as a 10 Gyr low-metallicity (1/20 solar) isochrone with $A_V = 0$. The orange cross marks the main-sequence turn-off (MSTO), while the orange point shows where a $2.2 M_\odot$ sub-giant branch star lies in color-color space for a solar metallicity 1 Gyr isochrone. The blue cross marks the MSTO and the blue point shows where a sub-giant branch $0.9 M_\odot$ star lies in color-color space for a 10 Gyr low-metallicity (1/20 solar) isochrone. We find that an $A_V = 18$ (shown by the green arrow in Figure 6) provides an adequate representation of the offset between the mean position of the colors of the cluster stars and the sub-giant branch of the isochrones. An $A_V = 18$ corresponds to an $A_J = 5.1$ according the relation given by Cardelli et al. (1989). The total range of extinctions across the ROI covering the standard deviation in the color-color distribution corresponds to $A_V = 14\text{--}22$.

Our analysis indicates a somewhat higher extinction compared to $A_V = 15 \pm 3$ found by previous studies (Kobulnicky et al. 2005; Ivanov et al. 2005). It is possible that the shallower surveys could not detect the sources with larger extinctions, leading to a bias in the extinction estimate. A ^{13}CO molecular cloud in front of the cluster (see Kobulnicky et al. 2005), is likely to be responsible for most of the extinction, including the differential extinction across the cluster. Indeed, the $24\mu\text{m}$ *Spitzer* MIPS image (see Figure 7) clearly shows the non-uniform ISM structure in the direction toward GC01.

4.3. Red Clump Stars

Red clump (RC) stars can be used to obtain an independent estimate of the distance to the cluster. For GC01, a clumping of stars from the red giant branch is seen around the apparent dereddened F153M magnitude of ≈ 11.2 (see Figure 8). In order to determine the distance corresponding to the magnitude at which the RC stellar distribution peaks, we use the dereddened apparent luminosity function of GC01 in the F127M and F153M filters (see Figure 8, for brevity we only show the luminosity function for the F153M filter). These filters

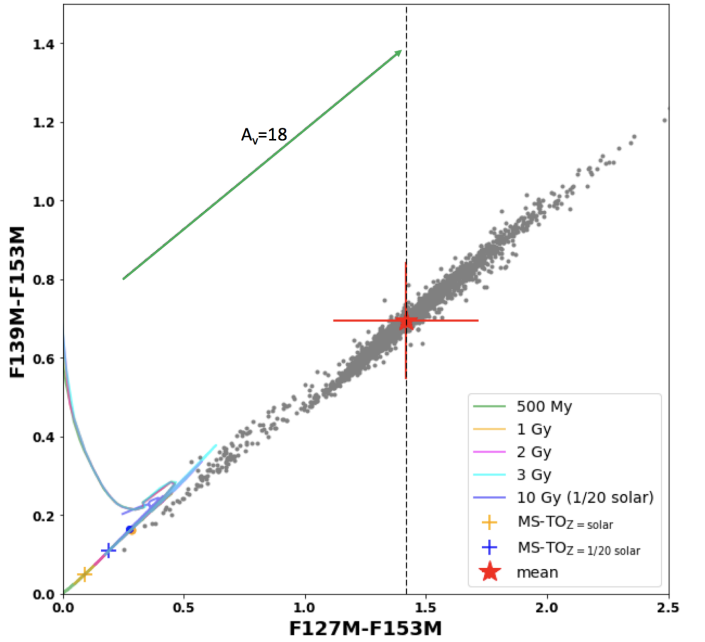


Figure 6. IR color-color diagram for all stars within the ROI that passed the quality cuts described in Section 2. The 500 Myr, 1 Gyr, 2 Gyr, and 3 Gyr solar metallicity, and the 10 Gyr low-metallicity (1/20 solar) isochrones with $A_V = 0$ are shown in green, orange, magenta, cyan, and blue, respectively. The red star shows the mean of the distribution, while the error bars show the 1σ standard deviation. The green arrow is the $A_V = 18$ reddening vector. The orange and blue crosses show the location of the main-sequence turn-off (MSTO) for the 1 and 10 Gyr isochrones, respectively. A $2.2 M_\odot$ star on the 1 Gyr isochrone is indicated by an orange point and a $0.9 M_\odot$ star on the 10 Gyr isochrone is shown as a blue point.

were chosen because they are the nearest to the Johnson J and H bands, where the red clump stars have well established absolute magnitudes (see Girardi 2016 and references therein). Therefore, the conversion from J and H magnitudes to F127M and F153M magnitudes are the least impacted by the assumptions about the RC stellar spectrum.

To convert between the HST and Johnson filters we approximated the RC stellar spectrum using a PL model ($F_\lambda \propto \lambda^\alpha$) with a spectral index of $\alpha = -1.9$, consistent with the absolute magnitudes provided in Laney et al. (2012). To ensure there are no broad absorption features in the RC stellar spectra at these wavelengths, we examined the corresponding Castelli & Kurucz stellar atmosphere models (Castelli & Kurucz 2004). The stellar atmosphere models with solar and low metallicities are well approximated at these wavelengths by the assumed PL model. The absolute¹⁵ J and H magni-

¹⁴ We use the extinction parameterization provided in Fitzpatrick (1999).

¹⁵ All stars in the Laney et al. (2012) sample were nearby and showed no signs of extinction effects.

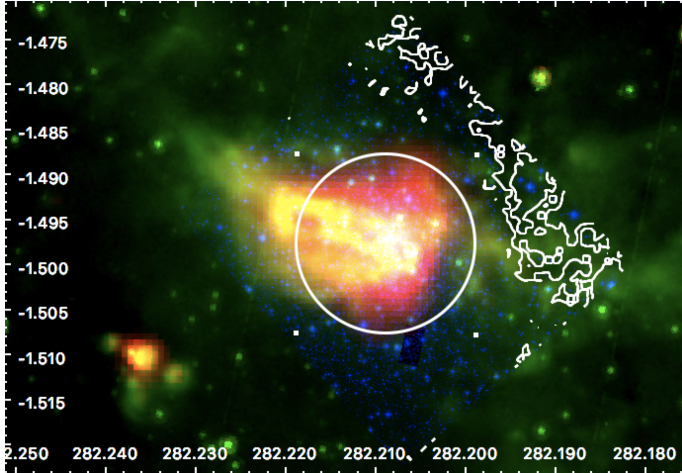


Figure 7. Three color image of the GC01 vicinity from the 24μ *Spitzer* MIPS (red), 8μ m *Spitzer* IRAC (green), and F127M filter HST (blue) data (North is up, East is to the left). The $36''$ white circle (half-light radius) is the same as in Figure 1. This image highlights the gas and dust across the cluster, which is the reason for the differential extinction affecting the CMDs (see Section 4.4). The white contours outline the dust lanes seen to the west of the cluster in Figure 2.

tudes of Laney et al. (2012) converted to the F127M and F153M bands are -1.02 and -1.45 , respectively¹⁶.

In order to measure the distance to GC01, we found the apparent dereddened ($A_V = 18$) magnitude of the RC stellar peak in the F127M and F153M luminosity functions. To ensure that the calculated distances were similar as a function of bin size, two different bin sizes (i.e., 0.1 and 0.2 magnitude per bin) were used. These two bin sizes were chosen to be small enough to capture the RC in the luminosity function, but large enough to have reasonably small statistical fluctuations per bin (see Figure 8). The apparent dereddened magnitudes corresponding to the RC are 11.57 – 11.62 for the F127M filter, and 11.10 – 11.19 , for the F153 filter. This corresponds to distances of 3.2 – 3.4 kpc. Reddening affects the distance derived from the RC position in the luminosity function. We repeated the above steps for $A_V = 17$ and $A_V = 19$ and found mean distances of 3.7 and 3.0 kpc, respectively.

We also compared the luminosity functions of GC01 including ($r < 42''$) and excluding ($18'' < r < 42''$) the cluster core and found an excess of RC sources in the core suggesting that there is mass segregation in GC01. However, the large extinction and crowding can lead to biases. Future observations with JWST can establish this much more confidently.

¹⁶ The magnitudes were converted using the power-law spectral model in pysynphot (Lim et al. 2015).

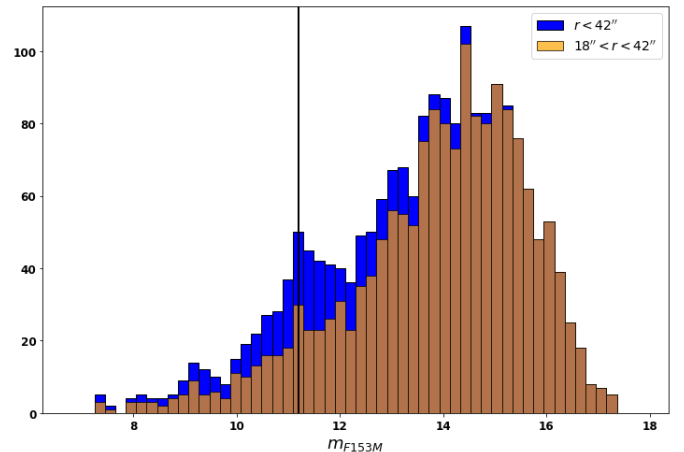


Figure 8. HST WFC3 F153M luminosity functions for all stars within the cluster ROI (blue) and excluding the cluster core $18'' < r < 42''$ (orange) with a 0.2 magnitude binning. The luminosity functions are extinction corrected for $A_V = 18.0$ (see Section 4.2). The peak of the red clump stellar distribution at $m_{F153M} = 11.19$, corresponding to a distance of 3.4 kpc (see Section 4.3), is indicated by a black vertical line.

4.4. Color-Magnitude Diagrams

In order to evaluate the contamination of the GC01 CMD by field stars we have defined a control field. Typically, this is done by imaging a flank field (see e.g., Andersen et al. 2017), however, such an observations does not exist for GC01. Therefore, we had to choose a region, as far as possible from the cluster center, in the western part of the WFC3 images where the fraction of the cluster’s stars appears to be minimal (orange rectangle in Figure 9). Additional complications arise due to the presence of the dark dust lanes within the western half of the control field region. This dust appears to be in front of the cluster, and therefore, most of the stars that are seen in that region are likely foreground to the cluster. The differences between the cluster and control field stars is evident in the F127M-F153M vs. F153M CMDs, shown in Figure 9. The crowding of sources in the dense cluster is apparent, as the photometric catalog goes ≈ 3 magnitudes deeper in the less crowded control field. The cluster stars lie primarily in the color space spanning $1.2 \lesssim F127M-F153M \lesssim 1.7$, while the foreground/background sources occupy a different region in color space. Based on Figure 9 the contamination from foreground/background sources plays a relatively small role in the CMDs above a F153M magnitude of 18 .

The left panel of Figure 10 shows the F127M–F153M vs. F153M apparent CMD together with 500 Myr, 1, 2, and 3 Gyr isochrones computed for solar metallicity and the 10 Gyr isochrone computed for $1/20$ solar metallicity. The isochrones are reddened with an $A_V = 18$ (see Section 4.2) and placed at $d = 3.3$ kpc (see Sec-

tion 4.3). The grey points are all WFC3/IR sources that pass the photometric cuts described in Section 3.2 and lie within the ROI. The representative photometric errors are shown as horizontal error bars near the right boundary of each CMD for different magnitude. For solar metallicity, the observed CMD is best matched by the 2 Gyr isochrone (Figure 10, left panel). This age estimate is in agreement with the one obtained by Davidge et al. (2016).

The 10 Gyr low-metallicity (1/20 solar metallicity) isochrone does not match the data well for this reddening and distance. However, for lower extinction ($A_V = 17$) the RC indicates a farther distance ($d = 3.7$ kpc) and the CMD is better matched by the 3 Gyr solar metallicity isochrone or the 10 Gyr low-metallicity isochrone (see Figure 10, right panel). Alternatively, for higher extinction ($A_V = 19$) the RC indicates a smaller distance ($d=3$ kpc; see Section 4.3), suggesting a younger age of ~ 1 Gyr. The large spread in the color of the stars is indicative of substantial (corresponding to $\Delta A_V \sim 5$) differential reddening across the cluster, previously noted by Kobulnicky et al. (2005), Ivanov et al. (2005), and Davidge et al. (2016). This spread can only be partially explained by the large amount of crowding in the cluster’s core and by the contamination from foreground/background sources.

We have also constructed an optical-NIR CMD using the drizzled WFC3/UVIS image for source finding (see Figure 11). This approach reduces the number of confused (blended) NIR sources at the expense of having significantly less sources in the CMD. This CMD is in some sense the cleanest photometry we can produce, because of the higher spatial resolution and stricter cuts (the sources included in this CMD must pass both the NIR and UVIS cuts described in Section 3.2). Most of the counterparts to the X-ray sources do not pass the strict photometric cuts and hence do not appear in this CMD. The stretched appearance of the RC in this CMD emphasizes the effect of the differential reddening and also shows that the cluster is unlikely to be younger than 1 Gyr.

White dwarf (WD) cooling curves could in principle be used to get an independent age estimate of the cluster (see e.g., Richer et al. 1998). To estimate the observed magnitude of WDs in GC01 we used the WD sample provided in Holberg & Bergeron (2006), observed in 2MASS’s J , H , and K bands. The J and H bands overlap with the WFC3/IR bands used in our observation (see Figure 1). We took the hottest source in the above-mentioned WD sample ($T_{\text{eff}} = 92970$ K, $d = 169$ pc, $J_{\text{mag}} = 15.303$, $H_{\text{mag}} = 15.604$) and placed it at the distance of 3.3 kpc with $A_J = 5.1$ and $A_H = 3.4$ (Cardelli et al. 1989). Converting from J and H bands to the F127M and F153M filters, this gives expected

apparent magnitudes of ~ 27 and ~ 25 , respectively¹⁷. Therefore, we do not expect to see any WDs belonging to the cluster in the IR/UVIS images, as the observations do not go deep enough.

4.5. Discussion of Distance and Age

Our distance estimates using RC stars implies a distance of ≈ 3.0 – 3.7 kpc depending on the absorption ($A_V = 17$ – 19), which is also consistent with the distances expected from the isochrone matching to the CMDs. This is at the lower end of previous distance estimates of 3.1– 5.2 kpc obtained from the ^{13}CO feature emission and extinction map (Kobulnicky et al. 2005) but more consistent with the 3.8 ± 0.7 kpc distance obtained using RC stars (Ivanov et al. 2005). The smaller distances leave open the possibility that the cluster is embedded in the ^{13}CO cloud at 3.1 kpc, which could help to explain the strong differential reddening. Although, a non-uniform cloud directly in front of the cluster can also give rise to a differential reddening across the cluster.

One of the most controversial properties of GC01 is its age. The isochrone matching to the cluster CMD suggests an age of ~ 2 Gyr assuming a solar metallicity, $A_V = 18.0$, and distance of 3.3 kpc. If the reddening is smaller ($A_V = 17.0$), then the data are also consistent with an older (~ 3 Gyr or 10 Gyr for solar or low metallicities, respectively) cluster age at $d = 3.7$ kpc. If GC01 does have a low-metallicity, it would then be more likely to be a a GC passing through the disk of the Galaxy, because low-metallicity GCs are typically found in the Galactic halo and not the Galactic disk (see e.g., Leaman et al. 2013). We find that ages ≤ 1 Gyr require a higher reddening $A_V=19$ and smaller distance $d = 3.0$ kpc. However, Kobulnicky et al. (2005) rule out distances < 3.1 kpc based on the extinction of the cluster, which requires it to be behind or overlap with the ^{13}CO cloud at $d = 3.1$ kpc. This implies that GC01 is older than 1 Gyr. The WFC3/UVIS CMD also disfavors ages < 1 Gyr.

Recently, Davidge et al. (2016) have fitted *SPITZER* IRAC CMDs and found the age to be between 1 and 2.5 Gyr, in good agreement with our estimate for solar metallicity. Thus, it is possible that GC01 is a 1–3 Gyr old massive cluster born in the Galactic disk with an age similar to those of the Galactic clusters IC 4651, NGC 752, and M67 (Meibom et al. 2002; Bell 1972; Mooley & Singh 2015) but with a much larger mass. Due to its large mass, it could be an aged YMC, such as Westerlund 1, RSGC 03, or Arches (Portegies Zwart et al.

¹⁷ The conversion was done using a flat spectral model (i.e., $(F_\lambda \propto \lambda^\alpha)$ with $\alpha = 0$).

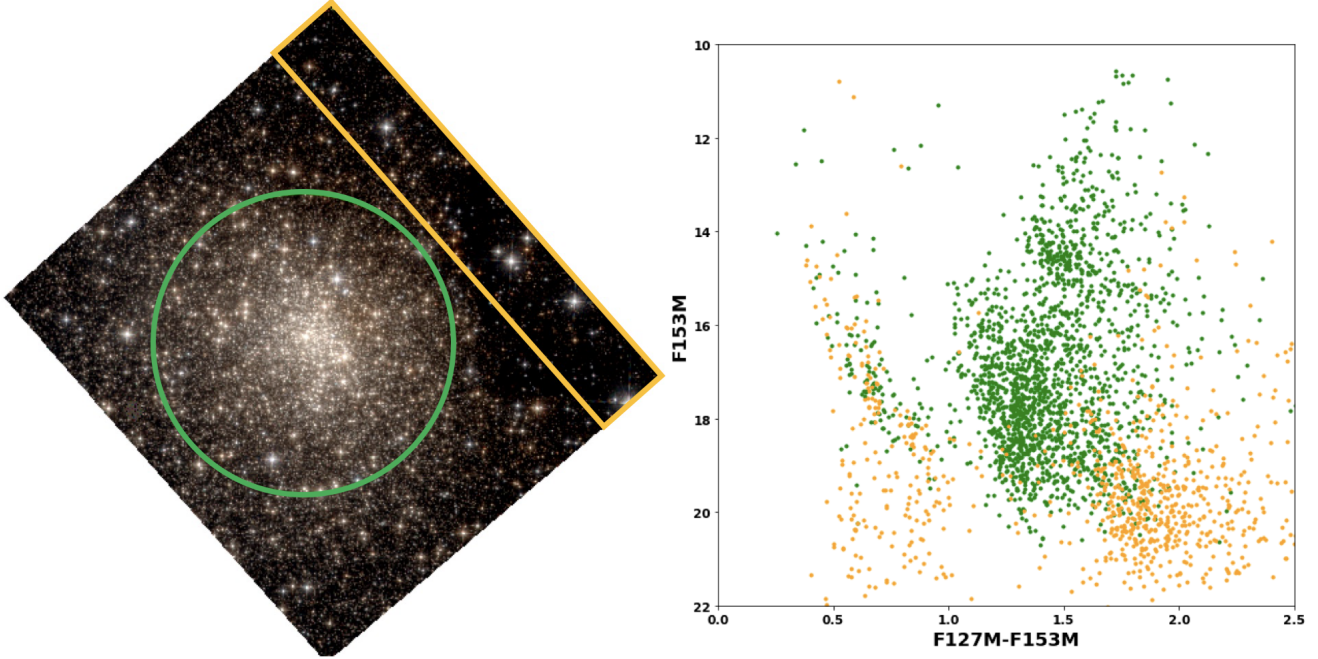


Figure 9. *Left:* False color WFC3/IR image (red: F153M, green: F139M, blue: F127M filters) image of GC01. North is up and East is to the left. The green circle shows the $r = 42''$ ROI used for our analysis. The orange box shows the control field region (Section 4.4). *Right:* The observed CMD (F153M vs. F127M–F153M) for stars within the ROI (green) and for the control field (orange). Cluster members tend to have F127M–F153M colors of ~ 1.2 – 1.7 . The ROI has an area ~ 2 times larger than the control field.

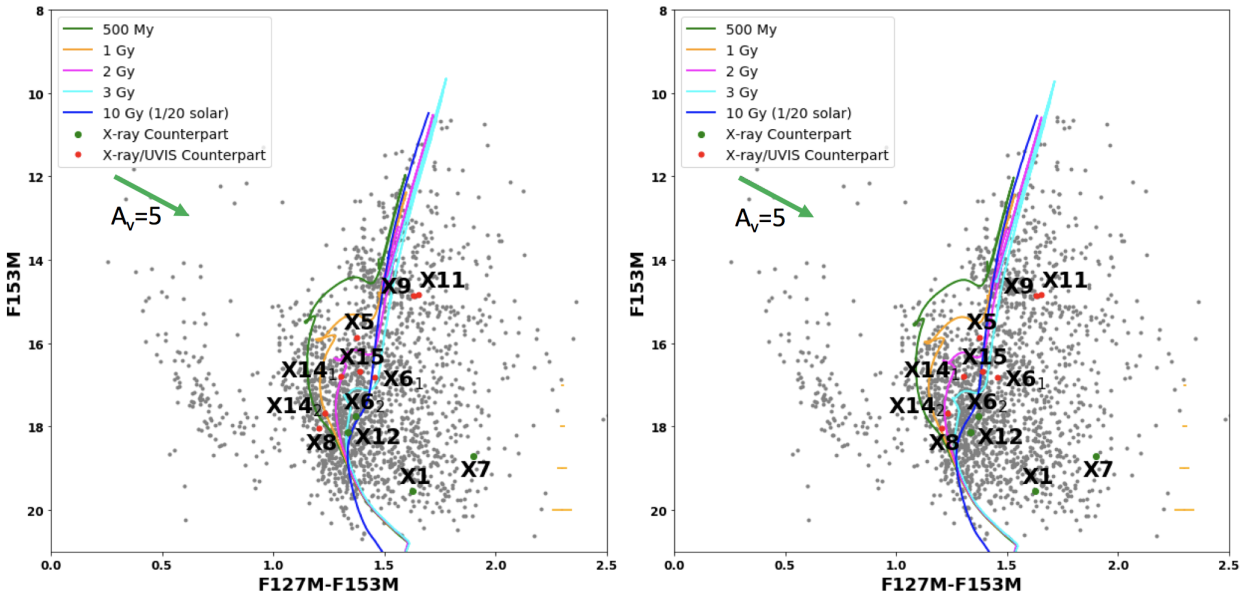


Figure 10. *Left:* Apparent WFC3/IR CMD (F153M vs. F127M–F153M) for stars within the $r = 42''$ ROI with solar metallicity isochrones from 500 Myr to 3 Gyr and a 10 Gyr low-metallicity (1/20 solar) isochrone over-plotted. The isochrones are reddened with $A_V = 18$, and placed at an assumed distance of 3.3 kpc. The mean photometric color uncertainties are shown as orange error bars for several different magnitude. The NIR counterparts to the X-ray sources are shown as colored (i.e., red or green) points and are numbered by a subscript if the X-ray source has multiple possible counterparts. The red points indicate that the source has both a WFC3/IR ($\text{SNR} > 30$) and UVIS ($\text{SNR} > 10$) counterpart, while the green points indicate that only a NIR counterpart is present. The green arrow shows a plausible differential reddening vector, $\Delta A_V = 5$. *Right:* Same CMD as in the left panel but with the isochrones reddened with $A_V = 17$ and placed at an assumed distance of 3.7 kpc (see Sections 4.2 and 4.4).

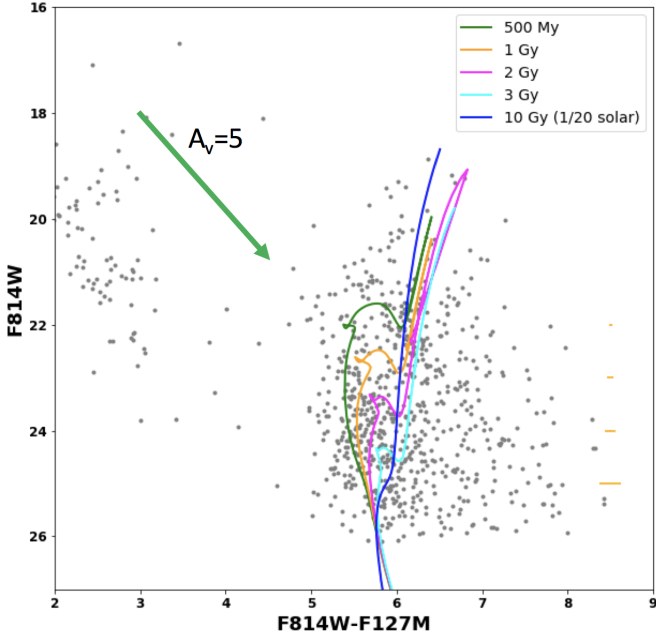


Figure 11. Observed WFC3/UVIS and IR CMD (F814W vs. F814W-F127M) for stars within $r = 42''$ ROI with solar metallicity isochrones from 500 Myr to 3 Gyr, and a 10 Gyr low-metallicity (1/20 solar) isochrone over-plotted. The isochrones are reddened with $A_V = 18.0$. A distance of 3.3 kpc is assumed. The mean photometric color uncertainties are shown as orange error bars for several different magnitude. The green arrow shows a plausible differential reddening vector, $\Delta A_V = 5$.

2010). However, with the data at hand, we cannot firmly rule out that GC01 is an old (~ 10 Gyr) low-metallicity globular cluster plunging into the disc. Future spectroscopic observations to determine the metallicity of GC01 would allow us to differentiate between these two scenarios. The higher angular resolution of *JWST* can also help to better constrain the properties of the CMD of GC01.

4.6. Loop-like Structure

Kobulnicky et al. (2005) reported a loop-like structure seen in the *Spitzer* IRAC images of GC01 from the *GLIMPSE* survey. They rule out both dust shells ejected by stars and a supernova remnant due to the size of the feature and lack of radio emission, respectively. They suggest that the structure could either be an old nova shell or planetary nebula (Kobulnicky et al. 2005). However, in the WFC3 images the structure is resolved into several stars of a similar brightness arranged in a peculiar loop-like pattern (see Figure 12), which can be described as an ellipse with a semi-major axis $a = 2''.7$ and semi-minor axis $b = 1''.7$, corresponding to physical sizes of 0.04 pc and 0.03 pc, respectively (at a distance of 3.3 kpc). If the structure is a ring seen in projection onto the sky, the inclination angle would be $\simeq 30^\circ$.

Only seven out of ~ 13 stars in the loop-like structure have photometry that satisfies the quality criteria of the photometric catalog. These seven stars are plotted as red points on top of our CMD. They all lie towards the top of the CMD (see Figure 12) and all but one have a F127M-F153M color of ~ 1.7 . Given the advanced age of the cluster it is difficult to imagine that the ring-like arrangement of the stars could be maintained since its formation. Most likely the structure is just an accidental arrangement in the projection onto the plane of the sky. Accurate 3D velocity measurements for these stars would provide further information. In addition to spectroscopic radial velocity measurements, future *JWST* observations would allow one to measure tangential velocity components of the stars if the cluster is as close as 3.3 kpc.

5. X-RAY SOURCES

Here we discuss the most interesting sources individually, based on their X-ray properties and the properties of their optical/NIR counterparts, while the remaining X-ray sources are discussed in bulk. We compare them to the X-ray source populations found in both old open and globular clusters. Nine of the 15 X-ray sources labelled in the left panel of Figure 2 have at least one NIR counterpart located within their X-ray positional error circles. The number of true counterparts is uncertain and can be smaller due to chance coincidence (see Section 3.3).

The unabsorbed 0.5–8 keV luminosities of the 15 X-ray sources span a range of $\sim 10^{31} - 10^{33}$ erg s $^{-1}$, with a majority having $L_X = 1\text{--}5 \times 10^{31}$ erg s $^{-1}$ (at $d = 3.3$ kpc). These luminosities are higher than those of flaring MS stars¹⁸ found in old clusters (see e.g., Giardino et al. 2008), implying that the detected sources can be a combination of ABs, MSPs (isolated or black-widow/redback type), CVs, and quiescent LMXBs, with the possible addition of more exotic source types, such as aged magnetars or old NSs accreting from the ISM (see Section 5.8).

Given the plausible 1–3 Gyr age of GC01, it could be that this cluster is an intermediate age cluster born in the disc. There are several open clusters with comparable ages that have been observed with CXO. M67 is an old open cluster with an age of 4 Gyr at a distance of 850 pc (Sarajedini et al. 1999). This cluster has been observed by both CXO and XMM-Newton and hosts a number of ABs of different types, as well as a CV (van den Berg et al. 2004; Mooley & Singh 2015). NGC 6791 is an older open cluster (8 Gyr) that lies

¹⁸ GC01 is too old to have any pre-main sequence stars or star-forming activity.

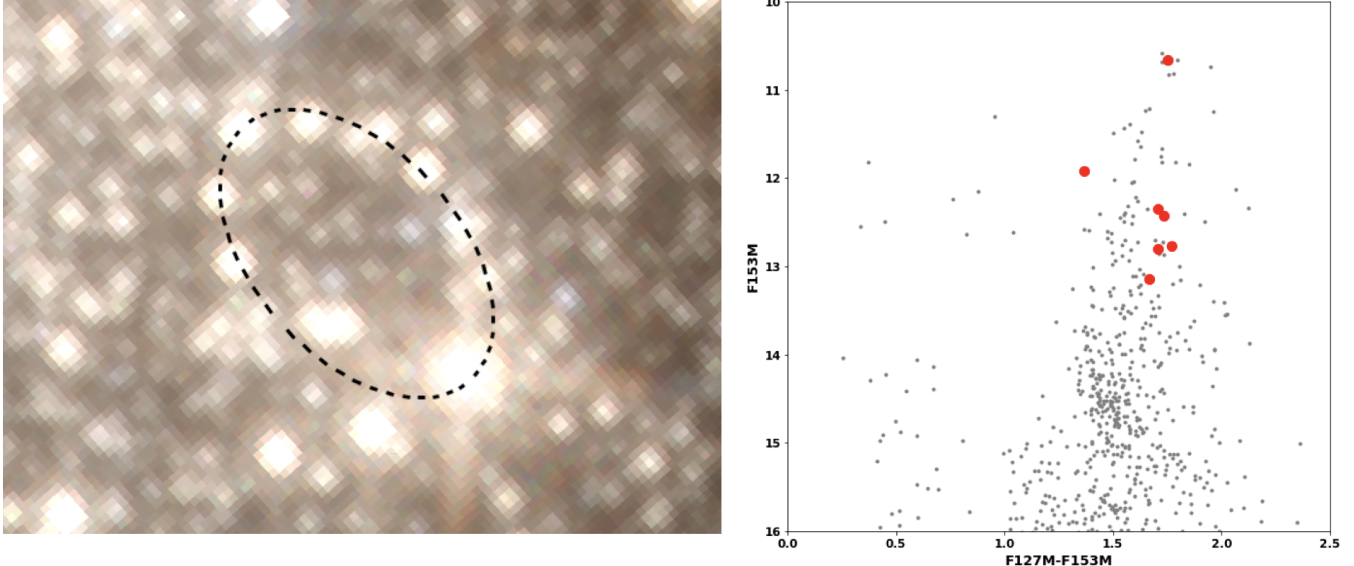


Figure 12. Left: HST WFC3/IR false color image in F127M (blue), F139M (green), and F153M (red) filters featuring the loop-like structure discussed in Section 4.6. Right: F153M vs F127M–F153M CMDs showing the locations (with the red filled circles) of the stars from the loop-like structure. The stars are bright, and lie on the red side of red giant branch of the isochrones.

at a comparable distance of 4 kpc and has a mass of 5000–7000 M_{\odot} (Platais et al. 2011; van den Berg et al. 2013), which is comparable to the mass of GC01 ($8000 \pm 3000 M_{\odot}$; Davies et al. 2011). NGC 6791 was observed with CXO and a number of X-ray sources, including ABs, CVs and binaries hosting sub-subgiants were detected with unabsorbed 0.3–7 keV luminosities ranging between $(1 - 15) \times 10^{30}$ erg s $^{-1}$ (van den Berg et al. 2013).

Alternatively, if GC01 has a low-metallicity and ~ 10 Gyr age, then it could be a GC passing through the Galactic disk. Many GCs have been observed with CXO, such as 47 Tucanae (Bhattacharya et al. 2017), ω Centauri (Haggard et al. 2009), Terzan 5 (Heinke et al. 2003) and M80 (Heinke et al. 2003). In comparison to old open clusters, GCs host more MSPs (see e.g., Bhattacharya et al. 2017) and qLMXBs (Heinke et al. 2003, Gosnell et al. 2012), while having fewer bright (i.e., $L_X > 1 \times 10^{30}$ erg s $^{-1}$) CVs, ABs, and sub-subgiants (SSG) per unit mass (van den Berg et al. 2013).

In ABs, the X-rays come from interacting magnetically active stars. The magnetic activity of these stars is enhanced due to a large rotation (i.e., periods on the order of 1–10 days van den Berg et al. 2004) maintained by tidal interactions with the companion star (Vats & van den Berg 2017). These sources typically account for a large fraction of the X-ray source population in old open clusters and often dominate their X-ray luminosity (see e.g., Vats & van den Berg 2017, van den Berg et al. 2004). The population of ABs in old open clusters have typical X-ray luminosities between 10^{28} – a few $\times 10^{31}$ erg cm $^{-2}$ s $^{-1}$ (Mooley & Singh 2015; Pooley

& Hut 2006), soft spectra with median photon energies $E_{\text{med}} \approx 1.5$ keV (Vats & van den Berg 2017), and orbital periods between 0.1–1000 days (van den Berg et al. 2004). GCs also contain ABs (typically with $L_X < 10^{31}$ erg s $^{-1}$), however, they have fewer per unit mass than open clusters (van den Berg et al. 2013). This is because the AB population likely scales with the primordial binary fraction, which is reduced in GCs (see Heinkel 2010 and references therein). GC01 may harbor many ABs, however, most of them will be too faint to be detected at our limiting luminosity.

Very little is known about the population of MSPs in massive open clusters. All known YMCs are too young to host MSPs spun-up by accretion. On the other hand, most known old open clusters are too scattered and probably do not have enough gravitational pull to retain isolated or even binary MSPs that acquire kicks from a supernova (SN) explosion (Gonzalez et al. 2011).

If GC01 is a GC then it could host MSPs, as GCs are known to be rich with them (e.g., Bogdanov et al. 2006; Prager et al. 2017). Typically, MSPs exhibit a thermal ($kT \approx 0.1 - 0.2$ keV) X-ray spectrum, but several also have a hard power-law component ($\Gamma = 1 - 1.5$) and may show orbital variability on times-scales of a few to tens of hours (see e.g., Bogdanov et al. 2006, 2011a; Linares 2014). However, due to the large absorption towards GC01, we would not detect the lower luminosity ($L_{0.5-8} < 1.5 \times 10^{32}$ erg s $^{-1}$) thermal MSPs in the existing data.

Quiescent LMXBs are another type of relatively faint X-ray sources expected in evolved stellar environments. Heinkel et al. (2003) studied ~ 20 qLMXB candidates

detected in nine different GCs and found an empirical lower limit of 10^{32} erg s $^{-1}$ on their X-ray luminosity. In X-rays, qLMXBs with NSs appear as fairly soft sources, due to the thermal emission from the NS (e.g., Table 2 in Heinke et al. 2003 and Figure 1 in Sonbas et al. 2018). There have also been a number of BH qLMXB candidates with $L_X > 10^{32}$ erg s $^{-1}$ recently discovered in GCs (see e.g., Chomiuk et al. 2013; Miller-Jones et al. 2015; Bahramian et al. 2017) based on their X-ray to radio luminosity ratios. While in quiescence, BH LMXBs often exhibit hard spectra ($\Gamma = 1 - 2$) making them similar to CVs, but a CV nature can be ruled out if a radio counterpart is detected (Bahramian et al. 2017). At fainter luminosities, (Armas Padilla et al. 2014) reported a confirmed BH qLMXB with $L_X = 8 \times 10^{29} - 1.3 \times 10^{31}$ erg cm $^{-2}$ s $^{-1}$ and a PL photon index $\Gamma = 2.1$. Therefore, qLMXBs with BHs may be detectable in the existing CXO observation of GC01, but are difficult to identify without deep X-ray and radio observations.

To better understand the nature of GC01's X-ray sources, we carried out spectral fitting and jointly evaluated the X-ray and NIR/optical properties of the brightest sources. Below we discuss the most interesting sources and the different classes they could belong to. Unfortunately, the *HST* and X-ray observations of GC01 are too short to search for periodicity associated with binary motion and the X-ray sources have too few counts to search for a spin period, or in many cases, fit the spectra. The orbital period of the system, along with the X-ray luminosity and spectral slope, can help to determine the nature of the source (see e.g., van den Berg et al. 2004) and deeper X-ray, NIR, and radio observations of GC01 should be undertaken.

5.1. Source X1

This source has 61 net counts and an observed X-ray flux of 3.6×10^{-14} erg s $^{-1}$ cm $^{-2}$. The spectrum is hard and can be described by an absorbed PL with $\Gamma = 0.9 \pm 0.3$ at a fixed $N_{\text{H}} = 4 \times 10^{22}$ cm $^{-2}$. The unabsorbed luminosity of X1 is $L_{0.5-8} = 9.1 \times 10^{31}$ erg s $^{-1}$ at $d = 3.3$ kpc. The X-ray luminosity and spectral hardness of X1 are consistent with a CV or qLMXB nature of the source. The best-fit Γ is smaller than typical MSP or qLMXB values, but the uncertainties are large. However, for an MSP scenario, the non-thermal luminosity is too large. X1 has an X-ray color ($X_{\text{color}} = -0.1$) and luminosity ($L_{0.5-6} = 7.0 \times 10^{31}$), which are representative of CVs according to Figure 1 of Pooley & Hut (2006), with ABs being less probable because they typically have lower luminosities and softer X-ray spectra.

X1 has only one NIR counterpart within the 2σ X-ray position error circle with no UVIS counterpart (see Fig. 3). The X-ray to NIR flux ratio, $f_X/f_{\text{F127M}} = 8.4 \times 10^{-2}$, is consistent with a CV interpretation (see Figure 14).

Unfortunately, X1 has a high crowding value and could be a mix of two or more faint sources, which would decrease the X-ray to NIR flux ratio.

5.2. Source X2

Source X2 is the brightest source detected in GC01 with an observed flux of 1.2×10^{-14} erg s $^{-1}$ cm $^{-2}$. Most of the flux is in the soft band, as evidenced by both its large photon index $\Gamma = 5.6 \pm 0.6$ and X-ray color $X_{\text{color}} = 2.1$. The unabsorbed X-ray luminosity is $L_{0.5-8} = 3.4 \times 10^{33}$ erg s $^{-1}$ at a distance of 3.3 kpc and $N_{\text{H}} = 4 \times 10^{22}$ cm $^{-2}$. In GCs, where qLMXBs are most commonly found Heinke et al. (2003), sources with luminosities $> 10^{32}$ erg s $^{-1}$ and soft X-ray spectra are typically qLMXBs (Heinke et al. 2006), but this source's X-ray color $X_{\text{color}} = 2.1$, places it far to the right of known qLMXBs (see Figure 1 in Pooley & Hut 2006). Allowing for a factor of 1.5-2 smaller N_{H} , consistent with the observed variable A_V , would make the spectrum harder and more consistent with a qLMXB.

In open clusters, qLMXBs are rare. However, a qLMXB has been found in NGC 6819, which has an age of ~ 2 Gyr (Gosnell et al. 2012), suggesting that qLMXBs are present in open clusters of these ages. Further, NGC 6819 has a mass of $\sim 2600 M_{\odot}$ and half-light radius of 3.3' (Kalirai et al. 2001), which corresponds to a diameter of 4.4 pc at its distance of 2.3 kpc (Basu et al. 2011). GC01 is more dense than NGC 6819, therefore, it could host dynamically formed LMXBs.

X2 has no NIR/optical counterpart within its X-ray positional error uncertainty. It is not uncommon for qLMXBs in globular clusters to have very faint optical counterparts (see Heinke et al. 2003). Additionally, the suggested counterpart of the qLMXB candidate in NGC 6819 has a UV magnitude of 19.75 (Gosnell et al. 2012), but NGC 6819 has a very low extinction E(B-V)=0.15 compared to GC01. Therefore such a counterpart would likely not be detectable in GC01.

5.3. Sources X5

Source X5 appears to have a single NIR counterpart, which is resolved by UVIS into two sources, one of which falls close to the center of X-ray error circle (see Figure 3). This source is also the brightest of the two, with SNR>10 in the F814W image, passing the UVIS photometric quality cut. It has an optical magnitude $m_{\text{F814W}}=24.2$, but its NIR magnitudes have very large crowding values. This source has an X-ray color $X_{\text{color}} = -0.3$, unabsorbed X-ray luminosity is $L_{0.5-6} = 3.4 \times 10^{31}$ erg s $^{-1}$ at a distance of 3.3 kpc, and X-ray to NIR flux ratio, $f_X/f_{\text{F127M}} = 1.1 \times 10^{-3}$ suggesting a CV nature of the source (however, see Section 5.8).

5.4. Source X8

Source X8 has a possible NIR ($m_{F127M}=19.2$) and optical counterpart ($m_{F814W}=24.0$). Of all the NIR/optical counterparts to the 15 X-ray sources, this one is the bluest ($m_{F814W} - m_{F127M} \approx 4.8$), lying on the blue side of the isochrones (see Figure 11). This source is also one of the furthest from the cluster center. It has an unabsorbed X-ray luminosity $L_{0.5-6} = 1.3 \times 10^{31}$ erg s $^{-1}$ and an X-ray color $X_{\text{color}} = -0.1$. Given the sources blue color and distance from the cluster center, X8 could be a foreground star.

5.5. Source X9

Source X9 has a potential NIR counterpart, which is bright ($m_{F127M}=16.5$) with well measured photometry. The source's position on the CMD suggests that this source could be a SSG or red straggler (RS) type star. SSGs and RSs lie on the redder side of the horizontal branch with SSGs being brighter and RSs being fainter than sub-giant branch stars (Geller et al. 2017). Typically, SSG and RS stars have X-ray luminosities of $10^{30} - 10^{31}$ erg s $^{-1}$ due to coronal magnetic activity (Geller et al. 2017). This source's X-ray color $X_{\text{color}} = 0.4$ and luminosity $L_{0.5-8} = 3 \times 10^{31}$ erg cm $^{-2}$ s $^{-1}$ are consistent with a SSG or RS type system. These types of sources have been found in both open and globular clusters (Geller et al. 2017). Spectroscopic follow-up would solidify the nature of this X-ray source.

5.6. Source X11

X11, reported as variable by Pooley et al. (2007), was only detected with ACIS during a 200-s flare and subsequent decay over the next 8 ks (see Figure 13). At its peak the flare reached a luminosity of $L_{0.5-8} = 2.1 \times 10^{33}$ erg s $^{-1}$ at a distance of 3.3 kpc. There is no NIR/optical counterpart within the 2σ X-ray positional error circle, however, there is a NIR source right on the very edge of the error circle. This source is bright ($m_{F127M}=16.5$), has reliable photometry, and lies very close to X9's counterpart in the CMD. This suggests it could also be an SSG or RS type system.

Most SSG/RS are found in binaries and they are not known to show flares with such high luminosities. However, a candidate qLMXB (based on its X-ray luminosity and a disputed 43.6 min periodicity; Heinke et al. 2001) in the GC NGC 6652, with quiescent X-ray luminosity of $\sim 10^{33}$ erg s $^{-1}$ and X-ray flares on time scales of 100 s reaching up to $L_{0.5-10} \lesssim 10^{35}$ erg s $^{-1}$, was suggested to host an SSG or RS (Engel et al. 2012; Geller et al. 2017). The qLMXB in NGC 6652 also shows optical variability on timescales < 75 s, making it difficult to reliably determine its color and firmly establish the SSG/RS nature of the donor star (Geller et al. 2017; Engel et al. 2012). X11 could be a similar type of qLMXB. Alternatively,

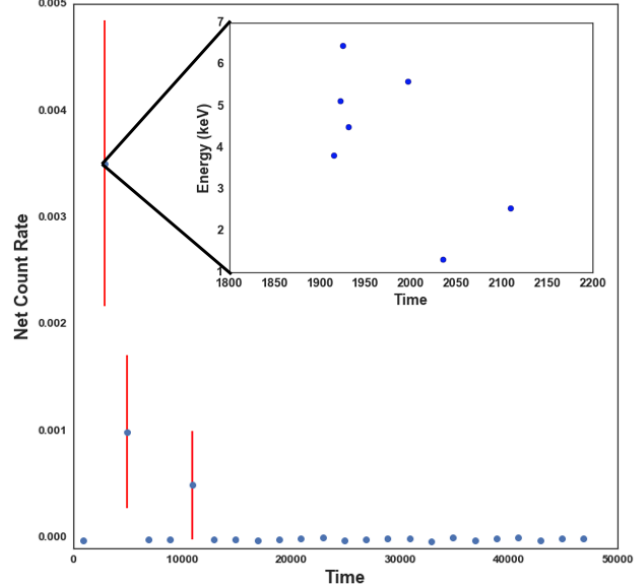


Figure 13. X-ray light curve with 2 ks bins for the only variable X-ray source (X11). The inset shows the energies of the photons arriving during the 200 s flare.

if the NIR source is not a true counterpart to X11, it could still be an LMXB with episodic accretion and a faint non-detected companion. Spectroscopic observations and further monitoring of this source are needed to firmly establish its nature.

5.7. Remaining Sources

The remaining eight X-ray sources have unabsorbed luminosities of $\sim 0.8 - 5 \times 10^{31}$ erg s $^{-1}$ at a distance of 3.3 kpc and X-ray colors between -0.8 and 0.4. Sources with $X_{\text{color}} < 0.0$ in this luminosity range tend to be CVs, while those with $X_{\text{color}} > 0.0$ can be a mix of ABs and binary MSPs (Pooley & Hut 2006).

In an attempt to classify these sources we have plotted the distance independent dereddened $J - H$ color versus the X-ray (0.5-7 keV) to J band flux¹⁹ ratio for the GC01 X-ray sources and candidate NIR counterparts (see Figure 14). We also plotted a number of CVs, MSPs, and LMXBs from various catalogs (see the Appendix of Hare et al. 2016 for more details) that have been detected by XMM-Newton (Jansen et al. 2001) and have counterparts in 2MASS. The X-ray fluxes and the J and H band photometry were retrieved from the 3XMM-DR6 catalog (Rosen et al. 2016) and 2MASS catalog of point sources (Cutri et al. 2003), respectively. Additionally, a sample of one globular and 10 open cluster SSG/RS type stars, which are detected at NIR (J and H bands) and X-ray wavelengths, was taken from Table

¹⁹ Both fluxes were corrected for absorption.

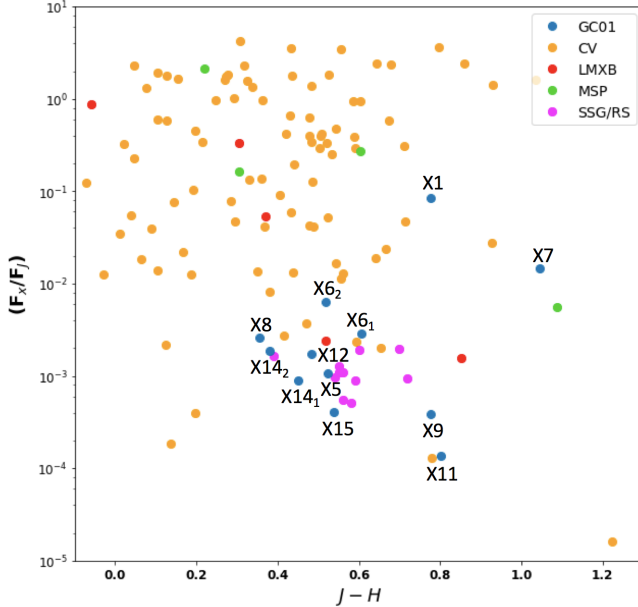


Figure 14. F_X/F_J versus $J - H$ color diagram. The candidate NIR counterparts to the X-ray sources were dereddened with an $A_V = 18$ and are plotted in blue. The CVs (orange), LMXBs (red), MSPs (green), and SSG/RS (magenta) have been taken from various catalogs and the literature and are all detected in X-rays and NIR (see Section 5.7). It should be noted that the colors can be very uncertain for NIR sources with large crowding values (see Table 3).

4 in Geller et al. (2017). For four MSPs²⁰, that have been detected by 2MASS and in X-rays, we converted the X-ray fluxes of the MSPs into the 0.5–7 keV energy range using the spectral models in the respective papers of each source (Bogdanov et al. 2011b; Zavlin 2006; Bogdanov et al. 2014; Zavlin et al. 2002). The F127M and F153M magnitudes of GC01’s NIR sources were converted to the J and H bands, respectively. The GC01 sources primarily fall near CVs and SSG/RS type stars in this plot. JWST will be able to better resolve stars in the crowded interior of the cluster and enable accurate NIR photometry.

There are large variations in the fraction of MSPs detected in X-rays among GCs. For instance, 47 Tuc hosts 25 radio MSPs, of which 22 ($\sim 90\%$) are detected in X-rays (see combined 540 ks CXO ACIS image in Bhattacharya et al. 2017). On the other hand, for Terzan 5 (combined 530 ks CXO ACIS exposure, see Figure 15) there are 36 known radio pulsars (Prager et al. 2017) of which only about 5 (or 14%) appear to be detected in X-rays (see Figure 15). The most likely reason for such a drastic difference is the much larger absorption ($N_H = 1 \times 10^{22} \text{ cm}^{-2}$ and $A_V = 6.7$) towards Terzan

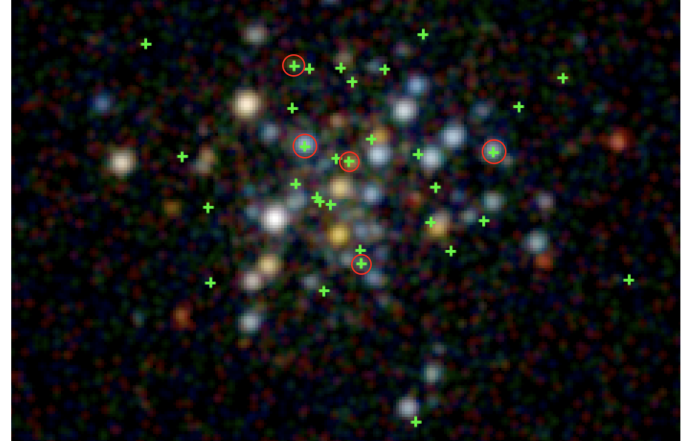


Figure 15. Merged 530 ks CXO false color image (3.0 – 8.0 keV - blue, 1.5 – 3.0 keV – green, and 0.5 – 1.5 keV – red) image of Terzan 5. North is up, East is to the left. The data are smoothed (with a Gaussian kernel with a radius of 2''.0). The green crosses show the radio positions of the MSPs reported in Prager et al. (2017), while the red circles highlight radio MSPs that are coincident with X-ray point sources. Most of the X-ray sources seen in this image are likely to be CVs and qLMXBs (see e.g., Heinke et al. 2006).

5, which is strongly affecting the detectability of the MSPs, most of which have thermally dominated spectra (see e.g., Bogdanov et al. 2006). Given that GC01 is even more obscured (by a factor of 4) than Terzan 5, it is not surprising that in the existing short CXO exposure we would see few or even no MSPs. The large absorption could also be affecting the ability to detect MSPs in radio (none have been found so far; S. Ransom, private comm.). Better quality X-ray and radio data for GC01 will allow us to directly compare the population properties of X-ray sources in Terzan 5 and GC01.

5.8. Intermediate mass BH limits

There have been theoretical predictions that intermediate-mass BHs (IMBH) could exist in the centers of GCs (see van der Marel 2004 for a review). Regardless of whether GC01 is an old open or globular cluster, it still has a very large core density and hence, may host an IMBH. If massive main sequence stars in GC01 undergo fast mass segregation, they can develop a Spitzer instability and N-body simulations show that this can lead to a core collapse time ~ 0.1 of the initial half-mass relaxation time (Gürkan et al. 2004). If the massive stars’ lifetimes are shorter than the core collapse time, the stars can collide and/or merge leading to a runaway collision process and, possibly, the formation of an IMBH (Portegies Zwart & McMillan 2002; Freitag et al. 2006). Portegies Zwart & McMillan (2002) find that clusters with present day half-mass relaxation times $< 10^8$ yrs and ages exceeding 25 Myr could contain an IMBH. N-body simulations predict that such an IMBH can have a mass of $\sim 0.1\%$ of the

²⁰ We could not use the large sample of MSPs detected in GCs because they do not appear in 2MASS and do not have NIR magnitudes.

birth mass of the cluster. Davies et al. (2011) estimate that the relaxation time of GC01 is $\sim 10^8$ yrs. Further, the current mass of GC01 could be as large as $\sim 80,000 M_\odot$, implying a birth mass up to an order of magnitude larger than its current mass (Davies et al. 2011). This suggests that a central IMBH could be as massive as $\sim 800 M_\odot$.

If there is an IMBH in GC01 it should accrete from the ISM in the cluster and may produce detectable emission. Emission from isolated stellar mass and IMBHs accreting at very low rates is poorly understood. X-ray observations of BH qLMXBs accreting at low rates show X-ray spectra which can be described as a PL with photon indices $\Gamma \approx 2$ (Armas Padilla et al. 2014; Plotkin et al. 2016). Starved supermassive BHs (such as Srg A*) seem to radiate most of their energy at sub-mm wavelengths (via synchrotron emission) with a possible second less energetic peak in X-rays due to inverse Compton (see Ponti et al. 2017 and references therein).

Since the putative IMBH would be in the cluster center, we consider X-ray sources X9 and X14, (lying 1-2'' away) as potential IMBH candidates. Source X9 is a likely SSG/RS type system, while source X14 has two potential NIR counterparts with photometry affected by the crowding. Source X5 is also only $\sim 4''$ away from the cluster center, but this source has a rather hard spectrum, making it a less likely IMBH candidate assuming the IMBH X-ray spectra are similar to those of low- L_X qLMXBs. All three sources have $F_X/F_J = 10^{-4}$ – 10^{-3} . Comparatively, Srg A* and the quiescent BH binary *Swift* J1357.2-0933 have X-ray to NIR flux ratios $F_X/F_J \approx 10^{-3}$ and 10^{-1} , respectively. Their X-ray luminosities are a tiny fraction of the Eddington luminosity, 10^{-8} – $10^{-9} L_{\text{Edd}}$ (Mossoux et al. 2016; Plotkin et al. 2016). An $800 M_\odot$ quiescent BH in GC01 with an X-ray luminosity of $10^{-9} L_{\text{Edd}} \approx 10^{32} \text{ erg cm}^{-2} \text{ s}^{-1}$ would have an absorbed X-ray flux $F_x = 3 \times 10^{-14} \text{ erg cm}^{-2} \text{ s}^{-1}$ (for $\Gamma = 2$, $N_H = 4 \times 10^{22} \text{ cm}^{-2}$), which would be detectable in the CXO observation. Deeper X-ray and NIR/IR observations (including NIR spectroscopy) are needed to probe the nature of X14, X9, and X5 to see if one of them could be an IMBH candidate in GC01.

6. OUTLOOK

There are two major obstacles in performing a more informative study of GC01. The first is the strong crowding in the cluster's core. This can be overcome with JWST's superior angular resolution, which will produce images with a quality comparable to that of the WFC3/UVIS F814W images. JWST will resolve sources that are too close together (such as the NIR counterpart to X5), provide accurate photometry, and be less affected by the large reddening. The second obstacle is the size of the X-ray error circles. Deeper X-ray

observations will allow us to detect more X-ray sources that can be cross-matched directly to HST and JWST sources and can then be used to improve the relative astrometry. This will reduce the X-ray position uncertainties allowing for more credible counterpart matching. Deeper X-ray observations would also better characterize the source spectra and allow for variability studies. It is important to understand the nature of the NIR and X-ray sources in GC01, as it may be only one of a few massive intermediate age clusters observable in the Galaxy and can provide hints to both its formation and evolution. Finally, it is critical to perform sensitive low-frequency radio observations to look for MSPs that are expected to be numerous if GC01 is an old GC.

7. SUMMARY

Using both *HST* and *CXO* we were able to probe the parameters of GC01 and its X-ray source population. We have detected 1,964 sources in the WFC3/IR F127M, F139M, and F153M images and 794 sources in the WFC3/UVIS F814W image. A color-color diagram suggests a variable extinction $A_V = 18 \pm 4$. The peak of the red clump star distribution was used to estimate the distance to the cluster, giving $d = 3.2$ – 3.4 kpc for $A_V = 18$. The CMDs and stellar isochrones corrected for this extinction and placed at a distance of 3.2–3.4 kpc imply an age of 1–3 Gyr. A lower metallicity would imply an older age (~ 10 Gyrs), a smaller extinction ($A_V = 17$), and a larger distance (3.7 kpc). Therefore, the *HST* photometry by itself does not confidently discriminate between an intermediate age massive galactic cluster or an old globular cluster plunging into the disk. The lack of any radio MSPs could suggest that GC01 is not an old GC (such as Terzan 5 or 47 Tuc), although there remains a possibility that their detections are hampered by the large absorption towards GC01.

We have analyzed the 15 brightest X-ray sources located within the central part of GC01. Nine of the X-ray sources have at least one NIR counterpart seen by *HST* and three have multiple NIR counterparts. Source X1 is a likely CV candidate given its X-ray colors and luminosity, but its NIR counterpart's photometry is not well measured. One of the sources (X2) is a likely a qLMXB as it has a soft X-ray spectrum ($\Gamma = 5.6$) and relatively large X-ray luminosity ($L_{0.5-8} = 3.4 \times 10^{33} \text{ erg s}^{-1}$). X9 has a NIR counterpart that has well measured photometry and lies in a region of the CMD that is often occupied by SSGs/RSs.

X11 does not have a NIR/optical counterpart inside of its X-ray positional error circle. However, there is one NIR/optical counterpart, with well measured photometry that lies in the SSG/RS region of the CMD, just on the edge of the X-ray positional error circle and may still be associated with X11. This source showed an

X-ray flare that lasted about 200 s and reached a peak X-ray luminosity of $L_{0.5-8} = 2.1 \times 10^{33}$ erg s $^{-1}$ and then decayed back to below the detection limit over 8 ks. A source, in the globular cluster NGC 6652, that has a similar X-ray luminosity and variability was suggested to be an LMXB with a possible SSG/RS companion Geller et al. (2017).

Acknowledgements: Support for Program number

HST-GO-14183.003-A was provided by NASA through a grant from the Space Telescope Science Institute, which is operated by the Association of Universities for Research in Astronomy, Incorporated, under NASA contract NAS5-26555. We are very grateful to Leisa Townsley and Patrick Broos for their help with running *ACIS Extract*, as well as for insightful discussions on X-ray image analysis.

REFERENCES

- Anders, E., & Grevesse, N. 1989, *GeoCoA*, 53, 197
- Andersen, M., Gennaro, M., Brandner, W., et al. 2017, *A&A*, 602, A22
- Armas Padilla, M., Wijnands, R., Degenaar, N., et al. 2014, *MNRAS*, 444, 902
- Arnaud, K. A. 1996, *Astronomical Data Analysis Software and Systems V*, 101, 17
- Basu, S., Grundahl, F., Stello, D., et al. 2011, *ApJL*, 729, L10
- Bell, R. A. 1972, *MNRAS*, 157, 147
- Bahramian, A., Heinke, C. O., Tudor, V., et al. 2017, *MNRAS*, 467, 2199
- Bhattacharya, S., Heinke, C. O., Chugunov, A. I., et al. 2017, *MNRAS*, 472, 3706
- Bogdanov, S., Grindlay, J. E., Heinke, C. O., et al. 2006, *ApJ*, 646, 1104
- Bogdanov, S., Archibald, A. M., Hessels, J. W. T., et al. 2011b, *ApJ*, 742, 97
- Bogdanov, S., van den Berg, M., Servillat, M., et al. 2011a, *ApJ*, 730, 81
- Bogdanov, S., Patruno, A., Archibald, A. M., et al. 2014, *ApJ*, 789, 40
- Bovy, J., Nidever, D. L., Rix, H.-W., et al. 2014, *ApJ*, 790, 127
- Broos, P. S., Townsley, L. K., Feigelson, E. D., et al. 2010, *ApJ*, 714, 1582
- Broos, P., Townsley, L., Getman, K., & Bauer, F. 2012, *Astrophysics Source Code Library*, ascl:1203.001
- Cardelli, J. A., Clayton, G. C., & Mathis, J. S. 1989, *ApJ*, 345, 245
- Castelli, F., & Kurucz, R. L. 2004, arXiv:astro-ph/0405087
- Chomiuk, L., Strader, J., Maccarone, T. J., et al. 2013, *ApJ*, 777, 69
- Coomber, G., Heinke, C. O., Cohn, H. N., Lugger, P. M., & Grindlay, J. E. 2011, *ApJ*, 735, 95
- Cutri, R. M., Skrutskie, M. F., van Dyk, S., et al. 2003, “The IRSA 2MASS All-Sky Point Source Catalog, NASA/IPAC Infrared Science Archive. [jA href="http://irsa.ipac.caltech.edu/applications/Gator/">](http://irsa.ipac.caltech.edu/applications/Gator/); <http://irsa.ipac.caltech.edu/applications/Gator/>”, *ApJS*, 132, 1221
- Cutri, R. M., Wright, E. L., Conrow, T., et al. 2012, Explanatory Supplement to the WISE All-Sky Data Release Products
- Davidge, T. J., Andersen, D. R., Lardière, O., et al. 2016, *AJ*, 152, 173
- Davies, B., Bastian, N., Gieles, M., et al. 2011, *MNRAS*, 411, 1386
- Dalcanton, J. J., Williams, B. F., Lang, D., et al. 2012, *ApJS*, 200, 18
- Dolphin, A. E. 2000, *PASP*, 112, 1383
- Dotter, A., Sarajedini, A., Anderson, J., et al. 2010, *ApJ*, 708, 698
- Engel, M. C., Heinke, C. O., Sivakoff, G. R., Elshamouty, K. G., & Edmonds, P. D. 2012, *ApJ*, 747, 119
- Evans, I. N., Primini, F. A., Glotfelty, K. J., et al. 2010, *ApJS*, 189, 37-82
- Freeman, P. E., Kashyap, V., Rosner, R., & Lamb, D. Q. 2002, *ApJS*, 138, 185
- Freire, P. C. C., Ridolfi, A., Kramer, M., et al. 2017, *MNRAS*, 471, 857
- Freitag, M., Rasio, F. A., & Baumgardt, H. 2006, *MNRAS*, 368, 121
- Fitzpatrick, E. L. 1999, *PASP*, 111, 63
- Foight, D. R., Güver, T., Özel, F., & Slane, P. O. 2016, *ApJ*, 826, 66
- Geller, A. M., Leiner, E. M., Bellini, A., et al. 2017, *ApJ*, 840, 66
- Giardino, G., Pillitteri, I., Favata, F., & Micela, G. 2008, *A&A*, 490, 113
- Girardi, L. 2016, *ARA&A*, 54, 95
- Gonzalez, M. E., Stairs, I. H., Ferdman, R. D., et al. 2011, *ApJ*, 743, 102
- Gosnell, N. M., Pooley, D., Geller, A. M., et al. 2012, *ApJ*, 745, 57
- Grindlay, J. E., Camilo, F., Heinke, C. O., et al. 2002, *ApJ*, 581, 470
- Gürkan, M. A., Freitag, M., & Rasio, F. A. 2004, *ApJ*, 604, 632
- Güver, T., & Özel, F. 2009, *MNRAS*, 400, 2050
- Haggard, D., Cool, A. M., & Davies, M. B. 2009, *ApJ*, 697, 224
- Hare, J., Rangelov, B., Sonbas, E., Kargaltsev, O., & Volkov, I. 2016, *ApJ*, 816, 52
- Heinke, C. O., Edmonds, P. D., & Grindlay, J. E. 2001, *ApJ*, 562, 363
- Heinke, C. O., Edmonds, P. D., Grindlay, J. E., et al. 2003, *ApJ*, 590, 809
- Heinke, C. O., Grindlay, J. E., Edmonds, P. D., et al. 2003, *ApJ*, 598, 516
- Heinke, C. O., Grindlay, J. E., Lugger, P. M., et al. 2003, *ApJ*, 598, 501
- Heinke, C. O., Wijnands, R., Cohn, H. N., et al. 2006, *ApJ*, 651, 1098
- Heinke, C. O. 2010, American Institute of Physics Conference Series, 1314, 135
- Holland, T. C. 2006, *ApJ*, 647, 1065
- Ivanov, V. D., Kurtev, R., & Borissova, J. 2005, *A&A*, 442, 195
- Jansen, F., Lumb, D., Altieri, B., et al. 2001, *A&A*, 365, L1
- Kalirai, J. S., Richer, H. B., Fahlman, G. G., et al. 2001, *AJ*, 122, 266
- Kharchenko, N. V., Piskunov, A. E., Röser, S., Schilbach, E., & Scholz, R.-D. 2005, *A&A*, 438, 1163
- Kiziltan, B., Baumgardt, H., & Loeb, A. 2017, *Nature*, 542, 203
- Kobulnicky, H. A., Monson, A. J., Buckalew, B. A., et al. 2005, *AJ*, 129, 239
- Kong, A. K. H., Bassa, C., Pooley, D., et al. 2006, *ApJ*, 647, 1065
- Krauss, L. M., & Chaboyer, B. 2003, *Science*, 299, 65
- Lan, S.-H., Kong, A. K. H., Verbunt, F., et al. 2010, *ApJ*, 712, 380
- Laney, C. D., Joner, M. D., & Pietrzyński, G. 2012, *MNRAS*, 419, 1637

- Leaman, R., VandenBerg, D. A., & Mendel, J. T. 2013, MNRAS, 436, 122
- Lim, P. L., Diaz, R. I., & Laidler, V. 2015, PySynphot User's Guide (Baltimore, MD STScI), <https://pysynphot.readthedocs.io/en/latest/>
- Linares, M. 2014, ApJ, 795, 72
- Lucy, L. B. 1974, AJ, 79, 745
- Manchester, R. N. 2017, Journal of Astrophysics and Astronomy, 38, 42
- Marigo, P., Girardi, L., Bressan, A., et al. 2017, ApJ, 835, 77
- Maxwell, J. E., Lugger, P. M., Cohn, H. N., et al. 2012, ApJ, 756, 147
- Meibom, S., Andersen, J., & Nordström, B. 2002, A&A, 386, 187
- Miller-Jones, J. C. A., Strader, J., Heinke, C. O., et al. 2015, MNRAS, 453, 3918
- Mishenina, T. V., Bienaymé, O., Gorbaneva, T. I., et al. 2006, A&A, 456, 1109
- Mooley, K. P., & Singh, K. P. 2015, MNRAS, 452, 3394
- Mossoux, E., Grosso, N., Bushouse, H., et al. 2016, A&A, 589, A116
- Pavlov, G. G., Kargaltsev, O., Garmire, G. P., & Wolszczan, A. 2007, ApJ, 664, 1072
- Platais, I., Cudworth, K. M., Kozhurina-Platais, V., et al. 2011, ApJL, 733, L1
- Plotkin, R. M., Gallo, E., Jonker, P. G., et al. 2016, MNRAS, 456, 2707
- Ponti, G., George, E., Scaringi, S., et al. 2017, MNRAS, 468, 2447
- Pooley, D., Lewin, W. H. G., Homer, L., et al. 2002, ApJ, 569, 405
- Pooley, D., & Hut, P. 2006, ApJL, 646, L143
- Pooley, D., Rappaport, S., Levine, A., Pfahl, E., & Schwab, J. 2007, arXiv:0708.3365
- Pooley, D. 2010, Proceedings of the National Academy of Science, 107, 7164
- Portegies Zwart, S. F., & McMillan, S. L. W. 2002, ApJ, 576, 899
- Portegies Zwart, S. F., McMillan, S. L. W., & Gieles, M. 2010, ARA&A, 48, 431
- Prager, B. J., Ransom, S. M., Freire, P. C. C., et al. 2017, ApJ, 845, 148
- Renaud, F., Agertz, O., & Gieles, M. 2017, MNRAS, 465, 3622
- Richer, H. B., Fahlman, G. G., Roswick, J., & Ibata, R. 1998, ApJL, 504, L91
- Rosen, S. R., Webb, N. A., Watson, M. G., et al. 2016, A&A, 590, A1
- Rowles, J., & Froebrich, D. 2009, MNRAS, 395, 1640
- Sarajedini, A., von Hippel, T., Kozhurina-Platais, V., & Demarque, P. 1999, AJ, 118, 2894
- Scholz, R.-D., Kharchenko, N. V., Piskunov, A. E., Röser, S., & Schilbach, E. 2015, A&A, 581, A39
- Skrutskie, M. F., Cutri, R. M., Stiening, R., et al. 2006, AJ, 131, 1163
- Sonbas, E., Dhuga, K. S., & Gogus, E. 2018, arXiv:1801.07107
- Spitzer, L., Jr. 1969, ApJL, 158, L139
- van den Berg, M., Tagliaferri, G., Belloni, T., & Verbunt, F. 2004, A&A, 418, 509
- van den Berg, M. 2013, 370 Years of Astronomy in Utrecht, 470, 251
- van den Berg, M., Verbunt, F., Tagliaferri, G., et al. 2013, ApJ, 770, 98
- van der Marel, R. P. 2004, Coevolution of Black Holes and Galaxies, 37
- Vats, S., & van den Berg, M. 2017, ApJ, 837, 130
- Zavlin, V. E., Pavlov, G. G., Sanwal, D., et al. 2002, ApJ, 569, 894
- Zavlin, V. E. 2006, ApJ, 638, 951